

**A Computer-Based Cascaded Modeling and
Experimental Approach to the Physical
Characterization of a Clinical Full-Field Digital
Mammography System**

by

Hetal Ved

A Thesis submitted to the Faculty of the
WORCESTER POLYTECHNIC INSTITUTE
in partial fulfillment of the requirements for the
Degree of Master of Science

In

Biomedical Engineering

By

October 2002

APPROVED BY:

Dr. Andrew Karellas, Research Advisor

Dr. C. Sotak, Thesis Committee

Dr. Robert A. Peura, Thesis Committee

Dr. Ross Shonat, Thesis Committee

ABSTRACT

This study characterizes the image quality parameters of a clinical full-field digital mammography system at various x-ray spectral conditions. The energy of the incident x-ray beam, the spectral characteristics, and breast thickness impact the physical performance such as the detective quantum efficiency of the system, thereby affecting the overall performance. The modulation transfer function, noise power spectrum were measured without the anti-scatter grid, and the detective quantum efficiency was calculated for different incident x-ray conditions. Detective quantum efficiency was also calculated with the anti-scatter grid placed above the detector to study its impact. Results indicate a substantial drop in the detective quantum efficiency with the anti-scatter grid under certain conditions. It was also determined that detective quantum efficiency decreases as x-ray beam hardening is increased.

An existing spatial frequency-dependent cascaded liner systems model previously described by other investigators is used to predict the detective quantum efficiency of the system for different target-filter combinations. This theoretical model is based upon a serial cascade approach in which the system is conceptually divided into a number of discrete stages. Each stage represents a physical process having intrinsic signal and noise transfer properties. A match between the predicted data and the experimental detective quantum efficiency data confirmed the validity of the model.

Contrast-detail performance, a widely used quality control tool to assess clinical imaging systems, for the clinical full-field digital mammography was studied using a

commercially available CDMAM phantom to learn the effects of Joint Photographic Experts Group 2000 (JPEG2000) compression technique on detectability. A 4-alternative forced choice experiment was conducted. The images were compressed at three different compression ratios (10:1, 20:1 and 30:1). From the contrast-detail curves generated from the observer data at 50% and 75% threshold levels, it was concluded that uncompressed images exhibit lower (better) contrast-detail characteristics than compressed images but a certain limit to compression, without substantial loss of visual quality, can be used.

ACKNOWLEDGEMENTS

I am very thankful to everyone who has directly or indirectly helped me in completion of my thesis. First of all I would like to thank my advisor Dr. Andrew Karellas for giving me an opportunity of working with him in the field of digital mammography. His continuous encouragement and support has made this thesis one of the most important projects I have ever taken up. I would like to thank Sankar Suryanarayanan and Srinivasan Vedantham. I have had a wonderful experience working with them in the lab. They have always been very inspiring throughout my thesis work. A lot of work was a joint venture between Sankar and myself and I would not have had such success without him. I would like to extend my special gratitude to Dr. Christopher Sotak, Dr. Ross Shonat and Dr. Robert Peura for being a part of the thesis defense committee and for their suggestions and guidance throughout my years of graduate study. I would like to thank Ina Lemon and Ruth Logan for their help whenever I needed it. I would like to thank Jay, Nimit, Ashish, Sumeet, Manish, Poorvi and Sanjay for giving me all the enthusiasm and support that I needed to achieve my goals. Finally, I express my gratitude to my parents and my sister, Hiral for their unconditional love and moral support throughout my graduate study, without which I would have never been the person I am today.

TABLE OF CONTENTS

	Page no.
Abstract	ii
Acknowledgments	iv
List of figures and tables	vi
Introduction	1
Background	6
Materials and Methods	15
Results and Discussion	34
Conclusion	60
References	63

LIST OF FIGURES AND TABLES

Figures:	Page no.
Figure 1: Illustration of the signal and noise transfer for gain and spreading stages as described in [14].	8
Figure 2: Wavelet transform as a tree of low-pass and high-pass filters.	13
Figure 3: The path of an incident x-ray photon in an indirect type of detector.	15
Figure 4: Flow chart summarizing the physical processes of a FFDM.	16
Figure 5: Effect of aliasing on the NPS (shown in one dimension).	21
Figure 6: Experimental setup for measuring the MTF.	24
Figure 7: Commercially available CDMAM phantom that was imaged using the FFDM for the contrast-detail study.	30
Figure 8: Predicted and experimental DQEs at 26 kVp, Mo/Mo and hardened by 20 mm, 45 mm and 60 mm Lucite are shown in (a), (b) and (c) respectively. The experimental DQEs were calculated using 1D NPS taken along the radial axis.	35
Figure 9: Predicted and experimental DQEs at 28 kVp, Mo/Rh and hardened by 20 mm, 45 mm and 60 mm Lucite are shown in (a), (b) and (c) respectively. The experimental DQEs were calculated using 1D NPS taken along the radial axis.	36
Figure 10: Predicted and experimental DQEs at 30 kVp, Rh/Rh and hardened by 20 mm, 45 mm and 60 mm Lucite are shown in (a), (b) and (c) respectively. The experimental DQEs were calculated using 1D NPS taken along the radial axis.	37
Figure 11: Predicted and experimental DQEs at 26 kVp, Mo/Mo and hardened by 20 mm, 45 mm and 60 mm Lucite are shown in (a), (b) and (c) respectively. The experimental DQEs were calculated using 1D NPS taken along the horizontal axis.	38
Figure 12: Predicted and experimental DQEs at 28 kVp, Mo/Rh and hardened by 20 mm, 45 mm and 60 mm Lucite are shown in (a), (b) and (c) respectively. The experimental DQEs were calculated using 1D NPS taken along the horizontal axis.	39
Figure 13: Predicted and experimental DQEs at 30 kVp, Rh/Rh and hardened	40

by 20 mm, 45 mm and 60 mm Lucite are shown in (a), (b) and (c) respectively. The experimental DQEs were calculated using 1D NPS taken along the horizontal axis.

Figure 14: Presampling MTF of the FFDM imager with no added Lucite at different target/filter combinations.	43
Figure 15: Simulated and measured Mo/Mo spectra obtained at 26 kVp and transmitted through 20 mm, 45 mm and 60 mm Lucite are shown in (a), (b) and (c) respectively.	44
Figure 16: Simulated and measured Mo/Rh spectra obtained at 28 kVp and transmitted through 20 mm, 45 mm and 60 mm Lucite are shown in (a), (b) and (c) respectively.	45
Figure 17: Simulated and measured Rh/Rh spectra obtained at 30 kVp and transmitted through 20 mm, 45 mm and 60 mm Lucite are shown in (a), (b) and (c) respectively.	46
Figure 18: Raw NPS of the system measured at 26 kVp, Mo/Mo and hardened by different thickness of Lucite.	47
Figure 19: Normalized NPS of the system measured at 26 kVp, Mo/Mo and hardened by different thickness of Lucite.	48
Figure 20: Quantum detection efficiency of CsI:Tl scintillator for all target/filter combinations.	49
Figure 21: DQE of the system measured at 26 kVp, Mo/Mo and hardened by different thickness of Lucite.	49
Figure 22: DQE of the system measured at 28 kVp, Mo/Rh and hardened by different thickness of Lucite.	50
Figure 23: DQE of the system measured at 30 kVp, Rh/Rh and hardened by different thickness of Lucite.	50
Figure 24: Raw NPS measured at 26 kVp, Mo/Mo with 45 mm of Lucite and a 'pre-grid' exposure of approximately 10 mR.	51
Figure 25: Normalized NPS measured at 26 kVp, Mo/Mo with 45 mm of Lucite and a 'pre-grid' exposure of approximately 10 mR.	52
Figure 26: DQE of the system measured at 26 kVp, Mo/Mo and hardened by using 45 mm Lucite.	52

Figure 27: DQE of the system measured at 28 kVp, Mo/Rh and hardened by using 45 mm Lucite.	53
Figure 28: DQE of the system measured at 30 kVp, Rh/Rh and hardened by using 45 mm Lucite.	53
Figure 29: DQE of the system measured at 26 kVp, Mo/Mo with anti-scatter grid and hardened by varying the thickness of Lucite.	54
Figure 30: DQE of the system measured at 28 kVp, Mo/Rh with anti-scatter grid and hardened by varying the thickness of Lucite.	55
Figure 31: DQE of the system measured at 30 kVp, Rh/Rh with anti-scatter grid and hardened by varying the thickness of Lucite.	55
Figure 32: Percent correct detection characteristics of a single observer are shown for the uncompressed images at 0.80 mm disk diameter.	56
Figure 33: Percent correct detection characteristics of a single observer are shown for the uncompressed and all images compressed using different compression ratios at 0.80 mm disk diameter.	57
Figure 34: Mean CD characteristics obtained at 50% threshold level for all the uncompressed and compressed images.	58
Figure 35: Mean CD characteristics obtained at 75% threshold level for all the uncompressed and compressed images.	58

Tables:

Table I: Average kVp values from the digital mammography database in University of Massachusetts Medical School.	23
Table II: kVp values that were used in the study.	23
Table III: Imaging system parameters that were used in the cascaded model for predicting the DQE.	41

1. INTRODUCTION

Screen-film mammography forms the standard diagnostic tool for breast cancer, which is the second leading cause of cancer mortality in women, with nearly one in eight women developing the disease. Mammography is the x-ray projection of the breast for screening and diagnosis of breast cancers. Although, advances in screen-film mammography and film processing techniques have contributed to the significant improvements in diagnostic image quality and offer excellent spatial resolution, they are limited in their dynamic range, contrast characteristics[1] and post processing capabilities. In the literature, the sensitivity of screen-film mammography reported is approximately 80% to 85% [2], but it may be significantly less in the dense breast as detection of very soft subtle tissue lesions in glandular background tissue is very difficult. Digital mammography is an x-ray examination of the breast that replaces the conventional screen-film image receptor with a solid-state device that enables electronic detection. High detection efficiency, high dynamic range, better contrast characteristics and post processing capabilities such as computer-aided diagnosis are the advantages of digital mammography[3,4] . The ability to alter the window level, window width, and magnification of digital mammograms displayed on monitors offers the potential to detect breast cancers more reliably. Digitally acquired images can also be transferred to other radiologists, thereby promoting telemammography.

Digital mammography should address the problems occurring in screen-film techniques, and remain as sensitive as or more sensitive than current screen-film

mammography systems. Studies have suggested that screen-film and digital mammography are equivalent[5].

The significant advances in digital mammography have motivated the development of a variety of innovative detector technologies such as amorphous silicon (a-Si), amorphous selenium (a-Se) and charge-coupled devices (CCDs)[6-8]. The a-Si and a-Se-based imagers may be generically characterized as flat-panel imagers as they all incorporate a two-dimensional matrix of thin-film switches. Siewerdsen *et al.*[9] has reported an empirical and theoretical analysis of the noise performance of AMFPs in diagnostic radiology. The results of the analysis suggested strategies for future improvements of this imaging technology. Several studies have shown the frequency-dependent[10] and frequency-independent[11] signal and noise performance measurements of different direct and indirect type detectors.

Amorphous silicon-based full-field flat-panel digital mammography (FFDM) imagers are currently being used clinically for digital mammography. Earlier investigations of a prototype version of an a-Si based FFDM (Senographe DMR, GE Medical Systems, USA) indicated encouraging physical characteristics[12,13].

This study characterizes the image quality parameters of a clinical FFDM system (Senographe 2000D, GE Medical Systems, Milwaukee, WI) at different target-filter combinations and beam hardening conditions. The energy of the incident x-ray beam, the spectral characteristics and breast thickness impact the physical performance such

as the detective quantum efficiency (DQE) of the system, thereby affecting the clinical performance of the system. In this study, we experimentally measured the incident x-ray spectra and compared them to theoretical simulations to validate the measurements, but only the experimentally measured spectra were used in the calculations of the DQEs. An anti-scatter grid is placed between the x-ray beam path and the patient that reduces effect of scatter on images resulting in better image contrast. However, using such a grid could potentially alter the noise conditions and ultimately the DQE of the system. Thus, the impact of using an anti-scatter grid on the noise power spectrum and the DQE were investigated for the FFDM system.

Noise performance of an x-ray imaging system limits the overall performance of that system. Therefore, a detailed knowledge of the former is essential during the development of a new technology. A frequency-dependent theoretical model, developed and described by Siewerdsen[9,14], was modified according to this study requirements to predict the DQE of the clinical FFDM system at different target-filter combinations and beam hardening conditions. The experimental DQEs were then compared to the theoretical DQEs.

Contrast-detail performance is a widely used quality control tool to assess clinical imaging systems using human and experimental observer models. Receiver operating characteristic (ROC) studies have indicated that the detection accuracy of micro calcifications by radiologists is significantly reduced if mammograms are digitized at 0.1 mm x 0.1 mm[15]. A study also showed that detection accuracy by computer

decreases as the pixel size increases[16]. It is evident that very high resolution digitization has to be used for mammograms in order to preserve the information in the image. For the FFDM system with 1914 x 2294 pixels with pixel pitch of 100 μm , a four-view mammogram study will provide 32 megabytes of digital data approximately. The transmission and archiving of such a large amount of data is therefore an important consideration in implementation of digital mammography. An efficient data compression scheme that can reduce the amount of data without degradation in diagnostic decisions will alleviate these problems. Lucier *et al.*[17] have studied the effects of wavelet compression and segmentation on digital mammograms and have reported that wavelets could be used to achieve high compression rates in mammographic images without losing small details such as microcalcification clusters. Observer performance over three different image modalities (MRI, CT and X-ray) has been studied and images from each modality were subjected to lossy compression using conventional JPEG and wavelet techniques, at certain compression quality settings. Their results indicated that for a particular compression quality setting, the perceived image quality was slightly higher for wavelet compressed images than for JPEG compressed images[18].

The objective of the contrast-detail characteristics is to study the effects of JPEG 2000 compression of mammograms on human visual detection. JPEG 2000 is a new image coding system that uses state-of-the-art compression techniques based on wavelet technology. This technique is currently being developed by the Joint

Photographic Experts Group (JPEG) committee and it complements the discrete cosine transform approach used in current JPEG compression.

2. BACKGROUND

A digital mammography system differs from the screen-film at the x-ray photon detection and processing level. It consists of a direct or indirect x-ray photon detector (versus a bucky system that holds the cassette with the x-ray film in a screen-film mammography system), analog-to-digital converters, image processors and high-resolution monitors. All these components impact the image quality.

In Flat Panel Imager technology, imaging pixels are deposited on large glass substrates. These pixels form a two-dimensional grid. Each pixel consists of a hydrogenated amorphous silicon (a-Si:H) thin-film switch; either a thin-film transistor (TFT), a single diode or a pair of diodes. This pixel is coupled to a sensor to ensure x-ray detection. The readout and processing of analog signals from the array is controlled by external electronics.

In direct detection, the active matrix is coupled to a thick photoconductor layer that converts the incident x-rays directly into electrical charges[19]. The charges are collected by an electrode and stored in a capacitor element and an image is formed by these stored charges. Technical difficulties arise in controlling the fabrication of sufficiently thick, stable silicon layers (a-Si) over large areas limit the use of amorphous silicon in direct detection. Amorphous selenium (a-Se) photoconductive layers are successfully used in direct electrical contact with an underlying flat-panel array.

In the indirect detection approach, a phosphor layer such as a structured scintillator or a screen is placed in contact with the active-matrix array[19]. X-ray interactions with the phosphor result in generation of visible light photons. The intensity of light emitted is a measure of the intensity of the x-ray beam incident on the surface of the detector. Photosensitive elements on the active-matrix array generate electrical charges proportional to the light produced by the phosphor and this charge is stored in the pixels of the array for read out.

Modulation transfer function (MTF), noise power spectrum (NPS) and the DQE of an imaging system define the performance of the device[19]. They are described below.

2.1 Cascaded linear systems analysis:

Signal and noise performance of an a-Si:H imager are modeled using a cascaded linear systems model[14]. This model described by Siewerdsen[14] requires that the system have a linear and shift-invariant signal response and stationary noise processes, expressed in terms of noise power spectrum. The imaging system can be represented as a series of discrete stages, where each stage represents either a quantum gain or spatial spreading (blurring) process. The physical imaging system determines the order of the stages. The relationship between the input and output signal and the noise properties is explained in detail by Siewerdsen *et. al.* It can be summarized as shown below.

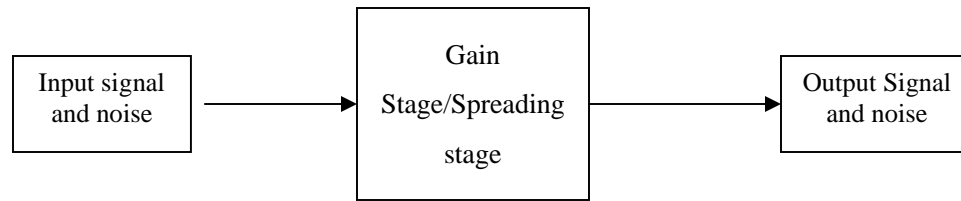


Figure 1: Illustration of the signal and noise transfer for gain and spreading stages as described in [14].

Each stage of a linear cascaded system is demonstrated by its signal properties in spatial coordinates and noise properties in spatial-frequency coordinates. The serial cascade of gain, spreading stages and additive noise where the output of one stage is the input of the subsequent stage, symbolizes an entire imaging system.

Quantum gain and spatial spreading stages are the two general types of stages in a system. Quantum gain stages, as the name suggests, describe the amplification of quanta (production of many optical quanta per absorbed x-ray photon) or loss of quanta (attenuation of optical quanta in traversing the phosphor medium). Spatial spreading stages describe either stochastic redistribution of quanta (homogeneous emission of optical photons from a phosphor grain) or deterministic redistribution of quanta (integration of optical photons by an aperture, where the photons are effectively redistributed to a single point at which they are counted).

2.1.1 Signal transfer properties of the gain and spreading stages:

The distribution of image quanta transferred to the output of a stage describes the signal transfer properties of the stage. For a gain stage, the mean fluence of the output quanta is :

$$\bar{q}_i = \bar{g}_i \bar{q}_{i-1} \quad (1)$$

where \bar{g}_i = mean gain [14]

\bar{q}_{i-1} = mean fluence [14]

A stochastic spreading stage changes the spatial distribution of the image quanta by randomly displacing each quantum by a distance with probability described by the normalized point spread function (PSF) in [14].

Random scattering of light photons in a scintillator before reaching the exit surface is one example of stochastic spreading and the signal transfer properties for integration of optical quanta by an aperture that represents a deterministic spreading stage.

2.1.2 Noise transfer properties of gain and spreading stages:

The noise transfer properties of the gain and spreading stages determine how the second-order statistics of the distribution of image quanta are transferred to the output. The noise transfer properties are described in detail by Siewerdsen[14].

Gain-variance is often expressed either in terms of the Poisson excess, ε , which the relative amount by which the gain-variance exceeds the Poisson distribution or in terms of the statistical (Swank) factor[20].

2.2 Modulation Transfer Function:

The modulation transfer function (MTF) of a system describes the spatial-response properties of the system. The MTF is the Fourier transform amplitude of the point spread function (PSF), which is the response of the system to a delta-function. Thus, MTF can be defined as :

$$\text{MTF}(u, v) = | \text{OTF}(u, v) | \quad (2a)$$

where $\text{OTF}(u,v)$ is the optical transfer function, the Fourier transform of PSF.

The various methods to measure the MTF are the square wave method, the edge method and the slit method. The composite MTF of a system included in [12] by Vedantham *et. al.* is the product of the MTF of all individual stages as these stages operate as filters on the image quality.

$$\text{MTF}(u, v) = \text{MTF}(\text{focal spot}) \times \text{MTF}(\text{presampled}) \times \text{MTF}(\text{slit}) \quad (2b)$$

Each component in equation (2b) is described in [12].

2.3 Noise Power Spectrum:

The noise power spectrum (NPS) can be defined as the variance of a given spatial-frequency component in an ensemble of measurements of that spatial-frequency. It can be shown that [12, 21]:

$$\text{NPS Raw}(u, v) = \frac{\langle | \text{FFT}(I - \text{mean}(I)) |^2 \rangle}{N_x N_y} \Delta_x \Delta_y \quad (3)$$

where I - image.

Δ_x and Δ_y - pixel pitch in x and y directions respectively.

N_x and N_y - number of elements in the x and y direction respectively.

Fixed pattern noise is eliminated from the NPS calculations by subtracting the mean of the average image or signal from every image.

2.4 Detective Quantum Efficiency:

The detective quantum efficiency (DQE) of the system is a measure of the effective fraction of incident Poisson-distributed quanta that contributes to the image signal-to-noise ratio (SNR). DQE can be given as [21]:

$$DQE(u, v) = \frac{MTF(u, v)^2}{\bar{q} \cdot NPS_{normalised}(u, v)} \quad (4)$$

2.5 Contrast-detail study:

The task presented to the observers is to detect the presence of a disc shaped object of known size and location in a noisy background. Statistical decision theory has been widely used to predict the dependence of threshold signal contrast on object size and many authors have used non-prewhitening (NPW) matched-filter to understand the CD behavior of imaging modalities[22-24]. A block diagram of the model is shown by Aufrichtig[22]. The model consists of the following components listed below.

The detection characteristics of a signal are affected by:

1. Imaging System - The spatial-response properties of the system and the spreading due to noise (NPS) make up the Imaging system.
2. Eye - Human Visual System Response

For a signal-known-exactly (SKE) problem, the threshold signal-to-noise (SNR_T) derived by Aufrichtig[22] is:

$$SNR = \frac{C_T}{A} \sqrt{q} F(u, v) \quad (5)$$

where C_T is the threshold contrast, $S(u,v)$ is the frequency response of the circular discs, $MTF(u,v)$ is the system modulation transfer function, $HVS(u,v)$ is the frequency response of the human visual system modeled as $HVS(f) = fe^{-\beta f}$ with a peak around 4 cycles/degree[25], $DQE(u,v)$ is the detective quantum efficiency, A is the large area signal, and q is the incident x-ray fluence.

Thus, the threshold contrast, C_T , required for object detection at a threshold can be calculated for the signal-to-noise ratio sufficient to pass that threshold in the observer model.

2.5.1 JPEG 2000 compression technique:

Compression techniques can be lossy or lossless. Lossless compression methods have the advantage that they can be applied to any image as such compressed images can be reconstructed without error. Their disadvantage is the small compression ratios, on the order of 3:1. In contrast, lossy techniques can achieve very high compression ratios at the expense of errors in the reconstructed images. The properties of human visual system are such that some losses can be tolerated without affecting the visual evaluation of an image, which, despite the losses, appears identical to the original.

JPEG 2000 compression supports both lossy and lossless compression. It uses wavelet technology in the lossy stage of image compression. Wavelets apply multi-resolution analysis to compress images. They separate the image data into different frequency components. Averaging of wavelets from a digital image corresponds to low-pass filtering and detail extraction of wavelets from the image corresponds to high-pass filtering operation. In other words, the low-pass filters reduce the amount of detail information in the signal, and the high-pass filters represent the information that is lost. The following tree diagram explains the effect of filtering. Consider a signal vector of length $n = 8$ (2^3). The filter operation will be:

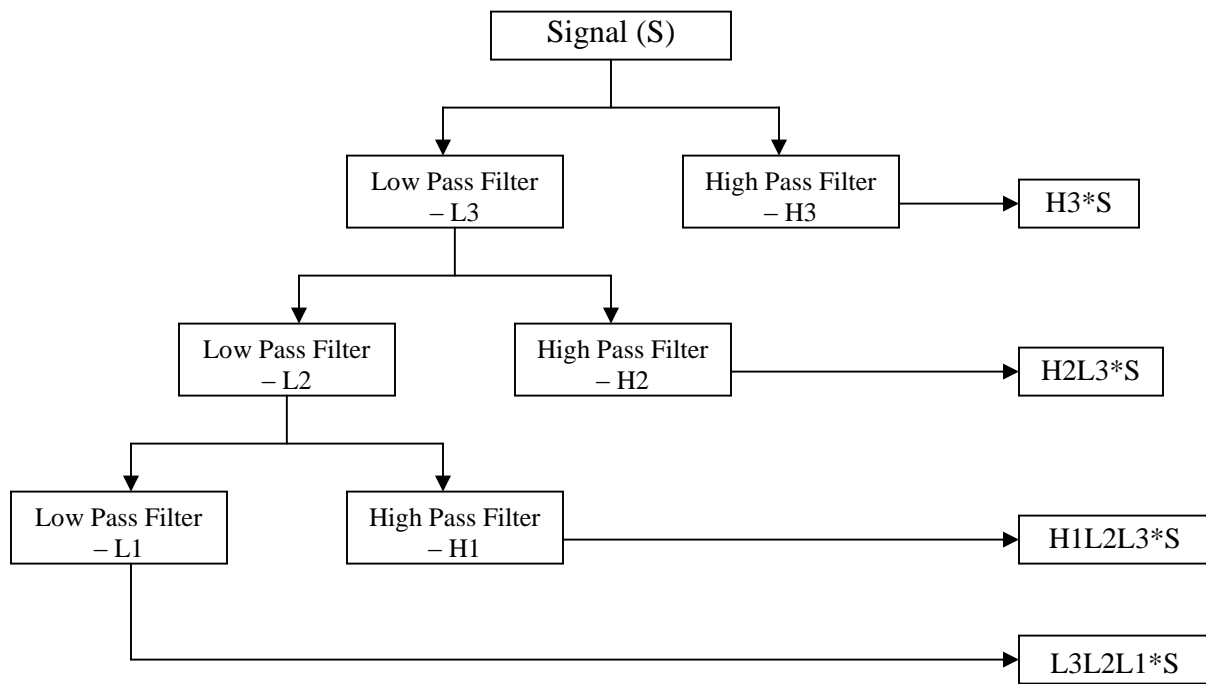


Figure 2: Wavelet transform as a tree of low-pass and high-pass filters. L_m and H_m represent the low-pass and high-pass filters at every stage [26].

The wavelet transform then consists of the final weighted average ($L3L2L1*S$) added to all the detail vectors collected at each step of the transform process. Hence, the wavelet transform is represented by

$$\{L3L2L1*S, H1L2L3*S, H2L3*S, H3*S\}$$

Multi-resolution wavelet representations give better performance because the wavelet basis functions are smoother than the DCT basis functions (which tend to be blocky even at low compression ratios), and are more natural and pleasing to the eye. JPEG 2000 supports progressive transmission and display of the image by transmitting lower resolution coefficients of the multi-resolution decomposition first. Basic geometric transformations can be applied on the compressed (using JPEG 2000) representation of the image.

3. MATERIALS AND METHODS

For a flat panel x-ray imaging system, the path of an incident x-ray photon can be traced from Fig. 4. X-rays when incident on the detector, interact in the scintillator to produce optical photons. These photons spread and are partially attenuated in the converter, while those that exit the screen form electron-hole (e-h) pairs which are collected by means of an applied signal. This contributes to the measured signal. The signal is then read out by switching the TFT to a conducting state via the voltage applied on the gate line. The data line carries the signal to the charge sensitive amplifiers, which integrate the signal outside the array. The analog signals are multiplexed, digitized and then sent to a computer.

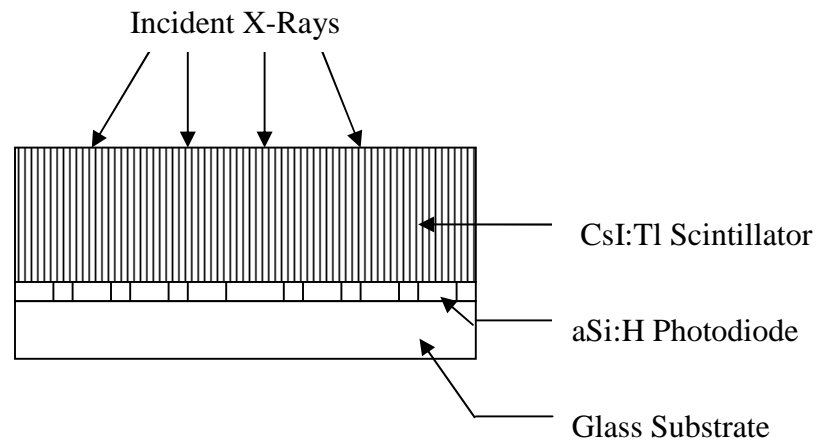


Figure 3: The path of an incident x-ray photon in an indirect type of detector.

3.1 The Serial Cascaded Model:

The full field digital mammography (FFDM) system and its physical processes can be summarized as shown in figure 4. Stage 0 describes the Poisson-distributed incident x-ray distribution; stage 1 represents the absorption of incident x-rays in the CsI:Tl

scintillator; stage 2 corresponds to the generation and emission of the optical photons in the scintillator; stage 3 represents the spread of the optical photons within the scintillator; stage 4 describes the coupling of these photons to the active matrix photodiode; stage 5 represents the integration of quanta by the photodiode sensor; stage 6 represents sampling of the detector signal from each pixel in the array; and stage 7 represents the readout stage. Electronic additive noise is added at stage 7. Each stage, either gain or spreading stage, is spatial frequency dependent. Each of the above stated stages is discussed in detail by Siewerdsen *et. al.*[9].

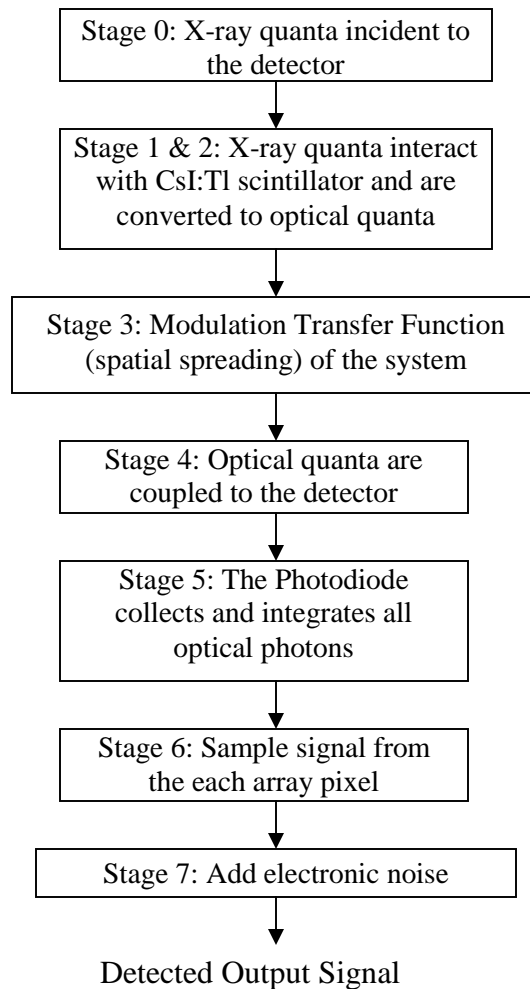


Figure 4: Flow chart summarizing the physical processes of a FFDM.

3.1.1 Stage 0: Incident x-ray quanta

The measured photon fluence for exposure of approximately 10 mR, is used in the model while predicting the DQE for the system. There is a loss in the flux[27] that reaches the scintillator due to the carbon and aluminum layers that are a part of the detector construction. The thickness of the carbon layer and the aluminum layer is 0.84 mm and 0.05 mm respectively. The linear density of carbon is 1.7 g/cm³ and that of aluminum is 2.699 g/cm³. The transmission factor was calculated as:

$$\begin{aligned} t &= \frac{I_1}{I_0} \\ &= I_0 \cdot e^{-(\mu(C).d(C).x(C)+\mu(Al).d(Al).x(Al))} \end{aligned} \quad (6)$$

where $\mu(y)$ are the linear attenuation coefficients; $d(y)$ are the densities (g/cm³); and $x(y)$ are the thicknesses (cm); y representing the different elements. I_0 is the measured normalized incident spectrum.

3.1.2 Stage 1: Interaction of incident x-ray quanta in the CsI:Tl scintillator

Stage 1 is a gain stage representing the interaction of incident x-ray quanta in the converting medium, CsI:Tl scintillator, where x-rays interact in such a way as to produce light. For an x-ray spectrum incident upon a converting material with interaction coefficient $\left(\frac{\mu}{\rho}(E)\right)$ and linear density d (g/cm³), the mean gain is calculated as described in Ref. [14].

3.1.3 Stage 2: Generation and emission of optical quanta

This stage summarizes the processes of generation and emission of optical quanta from the x-ray converter. These two processes can be either represented as a single stage with quantum gain \bar{g}_2 or as two separate substages, the optical gain (\bar{g}_{2a}) and the optical escape efficiency (\bar{g}_{2b}). The quantum gain \bar{g}_2 can be then given as:

$$\bar{g}_2(E) = \bar{g}_{2a}(E)\bar{g}_{2b}(E) \quad (7)$$

Eq. (8) is derived and explained in detail by Siewerdsen[14]

3.1.4 Stage 3: Spatial spreading of optical quanta in converting screen

The stochastic spreading of the optical photons in the converter, characterized by the screen MTF is described by Stage 3. This stage is frequency dependent. The MTF was approximated by a Lorentzian fit, also used by other authors[14, 28], to the measured data as:

$$MTF(Stage3) = \frac{1}{1 + H \cdot f^2} \quad (8)$$

where H is a fitting parameter that describes the blur of the screen.

3.1.5 Stage 4: Coupling of optical quanta

Stage 4 is a series of four sub-stages representing the coupling of optical quanta to the detector elements. Each of this sub stages follows binomial statistics.

The substages can briefly be explained as:

- a. Transmission through layers overlying photodiode

- b. Reflection at interfaces between overlying layers
- c. Absorption of photons in the photodiode and conversion of e-h pairs
- d. Collection of charge from the photodiode

3.1.6 Stage 5: Integration of optical quanta by photodiode

The integration of quanta by the photodiode represents a deterministic stage and is characterized by the presampling pixel MTF.

The pixel presampling MTF is given by the modulus of the sinc function[14]. The photodiode is assumed a square with $a_x = a_y = a$. Neighboring pixels do not share charge and effects of long range optical scattering are negligible too. The fraction of pixel area, $(\text{area of pixel})^2$, occupied by the area of the photodiode, a^2 , is given by[14]:

$$ffactor \equiv \frac{a^2}{\text{areaofpixel}^2} \quad (9)$$

where *ffactor* is called the fill factor.

The presampling MTF depends on the size of the photodiode aperture alone and is independent of the pixel pitch. Thus (for a fixed pixel pitch) increased fill factor (although increasing the mean pixel signal) actually degrades the presampling pixel MTF. But the process of sampling in stage 6 affects the signal and noise in a manner depending upon the pixel pitch; furthermore, the pixel fill factor will be seen to affect the amount of noise aliasing. Thus, improvements in fill factor tend to increase the mean pixel signal, decrease the presampling pixel MTF, and decrease the amount of aliased noise.

3.1.7 Stage 6: Sampling of the detector signal

Sampling of the detector signal from each array pixel is represented by this stage. This process is neither a quantum gain nor a spatial spreading stage, but it is included as a separate stage in the cascade to illustrate its presence in the processes of image formation. The assumption of the system being shift-invariant is violated at Stage 6 because the output of the stage can depend upon the location of the input. This violation can make the interpretations of the MTF, NPS and DQE complicated under conditions where the frequency content of the incident quanta is greater than the Nyquist frequency of the imager (i.e. the system is undersampled). The effect of aliasing on the NPS is calculated, which will represent this stage.

The sampling function, represented by a rectangular array of delta-functions with spacing equal to the pixel pitch, (area of pixel), in the spatial domain is described by Siewerdsen [14] as:

$$III(x, y) = \sum_{k, j=-\infty}^{\infty} \delta(x - k(\text{areaofpixel}), y - j(\text{areaofpixel})) \quad (10a)$$

Let u_{nyq} be the Nyquist frequency such as:

$$u_{nyq} = \frac{1}{2(\text{areaofpixel})} \quad (10b)$$

Depending upon the frequency content of the presampling signal, sampling of the signal causes aliasing of the signal and noise. In terms of the NPS, sampling causes noise power at frequencies above u_{nyq} to add to NPS below u_{nyq} . The aliased form, of the presampling NPS is hence given by Siewerdsen [14] as:

$$S_6(u, v) = S_5(u, v) ** III(u, v) \quad (10c)$$

Fig.5 illustrates the convolution process (in one dimension). The presampling NPS is replicated at multiples of the sampling frequency.

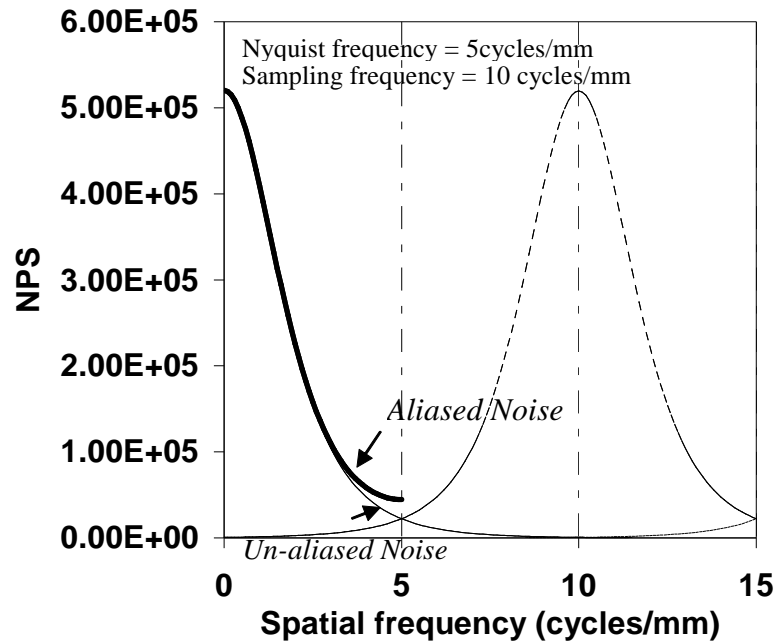


Figure 5: Effect of aliasing on the NPS (shown in one dimension). Noise components of sampled NPS below Nyquist (5 cycles/mm) are added to unaliased noise S_5 to produce aliased noise S_6 .

This concept is described by Siewerdsen[14]. The data plotted in the graph is produced from the theoretical model representing the Senographe 2000D system used for this work.

The effect of sampling is to increase the NPS as each replicant adds to the presampling NPS of the previous stage, to yield the aliased form.

3.1.8 Stage 7: Additive electronic noise

Additive noise is introduced in the process of signal readout, amplification and digitization. The total additive noise was added to the aliased NPS giving the final stage noise spectrum, which was then used to calculate the theoretical DQE. Additive

noise was calculated as the area under the two-dimensional NPS of the dark images[14] (images taken under no exposure) integrated over the Nyquist frequency limits.

3.1.9 Predicted DQE:

The frequency-dependent DQE was evaluated as:

$$DQE(f) = \frac{MTF^2}{q_0 \cdot NPS} \quad (11)$$

where q_0 is the number of photons per unit exposure (photons/mm²) after correction with the transmission factor.

3.2 Imaging System used for the study:

The clinical FFDM system (Senographe 2000D, GE Medical Systems, Milwaukee, WI) used in this study is composed of a 100 μ m thick thallium-doped CsI scintillator, an amorphous silicon photodiode array for indirect x-ray detection and special-purpose readout electronics. Light photons emitted from the interaction of x-ray photons in the scintillator traverse down the columnar crystalline structure of the scintillator, and are detected by a two-dimensional array of amorphous silicon photodiodes and thin-film transistors. The monolithic thin film flat panel array consists of a matrix with 1914 x 2294 detector elements of 100 μ m pixel pitch each. The electrical signal from each detector element or pixel is then read out and digitized to 16 bit digital values by low-noise electronics. The FFDM system uses a selectable dual track target, either molybdenum (Mo) or rhodium (Rh) with selectable filtration

of Mo or Rh. The tube voltages (kVp) used in the study were selected based on average kVp values computed from the digital mammography database at the University of Massachusetts Medical School (Table I).

Number of clinical Cases analyzed (LCC views)	Target/Filter	Average clinical voltage (kVp)
2051	Mo/Mo	26.42
2510	Mo/Rh	28.27
584	Rh/Rh	30.27

Table I: Average kVp values from the digital mammography database in University of Massachusetts Medical School.

The kVp values that were used in the experiments are shown in Table II. The tube current (mAs) was varied to maintain a clinically relevant incident exposure of approximately 10 mR for all the images used to compute the noise power spectra (NPS).

Target/Filter	kVp	Lucite thicknesses (mm)
Mo/Mo	26	20, 45, 60
Mo/Rh	28	20, 45, 60
Rh/Rh	30	20, 45, 60

Table II: kVp values that were used in the study.

3.3 Presampling modulation transfer function measurements:

The presampling modulation transfer function (MTF) was measured using the slit technique[29,30] at different target-filter and beam hardening conditions shown in Table II. The experimental setup for MTF measurement is as shown in Fig.6 .

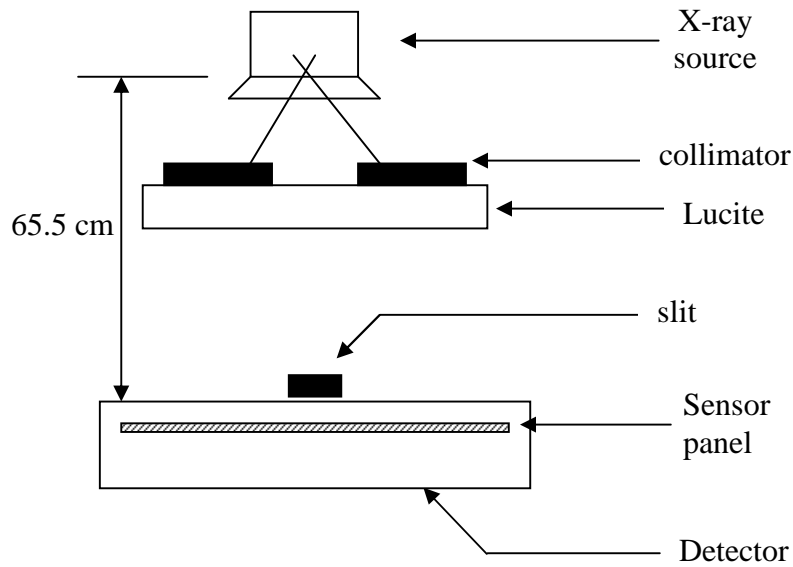


Figure 6: Experimental setup for measuring the MTF. A 10 μm slit is used for measuring the MTF. MTF was measured with and without Lucite in the path of the incident x-ray spectra.

A 10 mm long, 10 μm ($\pm 1 \mu\text{m}$) slit made of 1.5 mm thick tantalum was placed at a slight angle (less than 4°) to the anode-cathode-axis at the center of the detector. The area around the slit was covered with 0.5 cm thick lead (Pb). The slit was positioned approximately at the center and on top of the detector cover-plate (a few mm above the detector) as the anti-scatter grid and breast support plate were removed. The effects of blurring due to magnification were neglected because the source-to-detector distance was much larger than the slit-to-detector distance. The kVp values were fixed for a given combination of target-filter and lucite thickness while the mAs values were altered to acquire the tails of the dark subtracted line spread functions (LSFs) without significant electronic noise. The correction of variations along the edge of the slit was accomplished by normalizing the signal values along the horizontal direction (perpendicular to the anode-cathode axis) by dividing each pixel

value by the sum of the pixel values in that particular row. Pixel values were plotted along the vertical direction to obtain the number of individual LSFs needed to generate a finely sampled LSF[12].

The Fourier transform of the finely sampled LSF yielded corresponding MTF, which was then deconvolved of the finite dimension of the slit by dividing the resultant Fourier transform by a sinc function in the frequency domain to provide the presampling MTF. A total of nine presampling MTFs were obtained for the three Lucite thicknesses and three different target-filter combinations.

3.4 Noise Power Spectrum measurements without the anti-scatter grid:

The noise power spectra were measured for all the Lucite thicknesses and target-filter combinations without the anti-scatter grid at incident exposure of 10 mR. The clinical mammography system stores the acquired images as raw and processed images. Offset, gain and bad-pixel corrections are performed before the raw images are stored. Offset correction corrects for detector signal in the absence of any x-ray exposure by subtracting an offset image from an x-ray image. Gain correction corresponds to the correction of spatial variations in signal output per input x-ray exposure. Masking of bad-pixels using information from neighboring pixels results in bad-pixel correction. For each of the Lucite thickness and target-filter combinations, 16 images were acquired. A 1024 x 1024 region of interest (ROI) (mostly including the breast tissue area) was cropped and used in computing the average image. The

mean values of the signal in terms of digital units were computed from the respective average images. Subtracting the ROIs from their respective average ROI to obtain 16 difference images for each acquisition combination eliminated the fixed-pattern noise and structural effects. Four 256 x 256 ROIs were chosen from each difference images to obtain 64 ROIs for each of the nine acquisition combinations. Multiple ROIs were selected from each image for accurate estimation of the NPS. These ROI images were used to compute the ensemble average of the squares of the magnitude of the Fourier transformed images and the raw NPS was estimated [29] as shown in Eq. (12b).

$$\text{difference image} = \text{image} - \text{average image} \quad (12a)$$

$$NPS_{raw}(u, v) = \frac{\langle |FFT(\text{difference image}(x, y))|^2 \rangle}{N_x N_y} \Delta_x \Delta_y \quad (12b)$$

where Δ_x and Δ_y are the pixel pitch in x and y directions respectively ($\Delta_x = 100 \mu\text{m}$, $\Delta_y = 100 \mu\text{m}$) and N_x and N_y are the number of elements in the x and y direction respectively ($N_x = 256$, $N_y = 256$). Normalized NPS was then obtained using Eq. (3) [29].

$$NPS_{normalized}(u, v) = \frac{NPS_{raw}(u, v)}{(\text{mean signal of average image ROI})^2} \quad (12c)$$

An additional factor of $N/(N-1)$, where $N = 16$ represents the number of images that were averaged, was used to scale the normalized NPS to correct for the loss in variance introduced due to the background subtraction procedure. A two-dimensional (2D) NPS was finally obtained that excluded the fixed pattern noise of the detector. One-dimensional (1D) NPS was obtained by averaging the 2D NPS radially, the frequency value being $f = \sqrt{u^2 + v^2}$ for the 1D NPS estimate.

3.5 Noise power spectra measurements with the anti-scatter grid:

The NPS measurements for this part of the study were performed in an identical manner to the procedure described for measurements without anti-scatter grid, the only difference being that an anti-scatter grid was placed above the detector. Initially, the NPS was measured after filtering the x-ray beam through 45 mm Lucite with a pre-grid exposure of approximately 10 mR for all the three target-filter combinations. But since the grid had a bucky factor of 2, the post-grid exposure was reduced to nearly half the pre-grid exposure. In order to maintain a post-grid exposure of nearly 10 mR, the pre-grid exposure levels had to be nearly doubled. The average signal value to the detector was measured without the use of the anti-scatter grid. The anti-scatter grid was then used and an exposure level resulting in a similar signal value as the condition without the grid was used for all target-filter and Lucite thickness combinations.

3.6 Spectra Measurements:

The x-ray spectral distribution, $q(e)$ was characterized for the measurement conditions shown in Table II. Spectral simulations were performed for all nine conditions using the software and catalogued data provided by the Diagnostic Radiology and Magnetic Resonance Special Interest Group of the Institute of Physics and Engineering in Medicine[31]. The tables provided in this catalogue rely on the tube modeling method of Birch and Marshall[32]. A 0.8 mm Beryllium window and 25 μm Molybdenum or 30 μm Rhodium filter were assumed to simulate incident

spectra. Additional filtration was attained by addition of appropriate Lucite thicknesses into the model. The anode angle was 0° and the emission angle was assumed to be about 15° at the center of the detector[27].

The incident spectra were experimentally measured for all the spectral conditions. For each of the nine conditions, fifteen spectra were measured using a cadmium zinc telluride (CZT) based high-resolution spectrometer (XR-100T-CZT, Amptek, Inc., USA) and averaged to improve the precision of measurement. This yielded a total of nine averaged spectra. In addition to this, post-grid spectral measurements were performed with the anti-scatter grid in place over the detector. Since the energy absorption efficiency of the 3-mm-thick CZT spectrometer is more than 99.9% for the energy range (5-35 keV) of the incident spectrum, corrections for the spectrometer energy response was not required. The incident exposures at the surface of the detector for each spectral measurement were kept nearly same as the exposures used for NPS measurements. The exposures were measured with a calibrated mammographic ionization chamber connected to MDH 1515 (RadCal Corp., USA) dosimeter. The total number of photons incident per unit area of the detector were computed as[12,29]:

$$q = \frac{\int q(e)Y(e) de}{\int q(e) de} \quad (13)$$

where $Y(e)$ is the photon fluence per mR described by a polynomial that best fits to published values between 5 to 35 keV[19].

3.7 Detective quantum efficiency measurements:

To compute the frequency dependent detective quantum efficiency, DQE(f), NEQ(f) was first calculated from the system MTF and $NPS_{\text{normalized}}(f)$ as :

$$NEQ(f) = \frac{MTF^2(f)}{NPS_{\text{normalized}}(f)} \quad (14a)$$

As the additional lucite filtration did not degrade the detector MTF, MTF(f) used in the above computation was the MTF of the detector measured without any added lucite for each of the three target-filter combinations. The DQE was then computed using the NEQ(f) and the number of x-ray photons incident on the detector per unit area, q, as :

$$DQE(f) = \frac{NEQ(f)}{q} \quad (14b)$$

The DQE(f) using normalized NPS(f) with anti-scatter grid was calculated for both pre-grid and post grid 'q' values in order to assess the impact of the grid on the frequency dependent DQE characteristics of the system.

3.8 Contrast-detail study:

3.8.1 Contrast-detail phantom:

A commercially available contrast-detail phantom (CDMAM phantom; Nuclear Associates, Carle Place, NY) was used as the test object to study the effects of compression on the digital images.

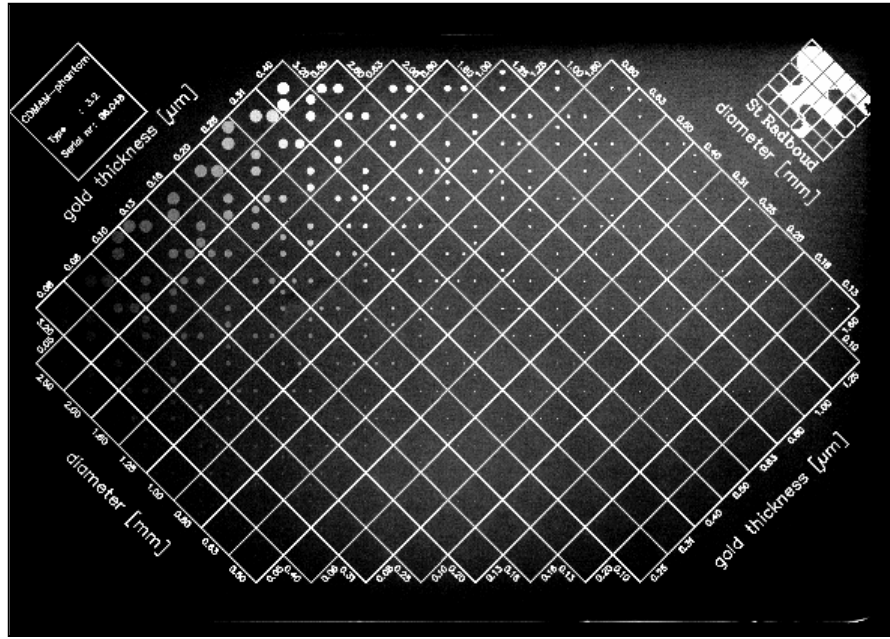


Figure 7: Commercially available CDMAM phantom that was imaged using the FFDM for the contrast-detail study. The 16 x 24 cm phantom consists of gold disks that vary in diameter and depth along the columns and rows respectively.

The phantom consists of a 0.5-mm-thick aluminum base, 16 x 24 cm in area, containing circular gold disks that are logarithmically sized from 0.10 to 3.20 mm in diameter and 0.05 to 1.6 μm in thickness. The disks are centrally placed within a matrix of squares forming 16 rows and 16 columns. For a given row, the thickness is constant with logarithmically varying diameter. A disk is randomly placed at one of the corners of each square and has the same thickness and diameter as the central disk in that square. This allows one to perform a four-alternative choice (4-AFC) detectability experiment. For this study, additional acrylic was used to bring the total thickness of the phantom to 5 cm while the actual thickness was 4.5 cm. This thickness is consistent with the mean compressed breast thickness of 5.1 cm computed from 4510 cases from our mammography database.

3.8.2 Image Acquisition:

All the images were acquired with the clinical FFDM system. Sixteen images of the phantom were acquired at 29kVp, 50 mAs. Only ten images from the sixteen acquired were used in the study. The images were cropped using IDL 5.5 (tool of the Research Systems Inc., Boulder, CO) such that only 3 columns, with disk diameters 1.0 mm, 0.8 mm and 0.63 mm, and 9 rows, with disk depths ranging from 0.05 μm to 0.31 μm , were displayed. The images were then compressed using Image Power's Power Compressor 1.5, a powerful images compressor and image management tool. JPEG2000 compression was achieved at 10:1, 20:1 and 30:1 compression ratios. Four sets (uncompressed, 10:1 compressed, 20:1 compressed and 30:1 compressed) of 10 images each were randomly displayed to the observers for the study. Display adjustment using window and level functions was used to enhance the digital images. These levels were kept constant for all the observers.

3.8.3 Observer study:

A total of six observers were used in the study and each observer independently reviewed the four image sets in a single session in a dark room. The images were cropped because it helped to maintain reasonable observation times (about 1 to 2 hours) and adequate data range for comparison was obtained too. The objective of the study was not told to the observers and the images were presented to the observers in a random fashion to reduce systematic errors.

A 4-AFC experiment was conducted as the CDMAM phantom has four-alternative choices presented by each square with a randomly located corner disk. The observers were asked to read one column at a time, starting with the largest diameter and proceeding towards the smallest perceivable disk in that column. Since this was a forced choice study, they were asked to arrive at their ‘best estimate’ for the location of the disk in each square in situations where the disks were not perceivable. A template representing the portion of the CDMAM phantom image under observation was provided and the observers were asked to mark the location of the corner disk in each square on this template. The observers were asked to refrain from looking at prior marked sheets to circumvent learning effects.

3.8.4 Data Analysis:

A signal detection model[33] was used to analyze the 4-AFC data. The model hypothesizes a continuous decision variable internal to the observer with Gaussian probability density functions for the choices: “disk present” and “disk absent”. The distance between the means of these two overlapping distributions is $d' = uC$, where C is the disk contrast and u is a parameter to be determined. As u increases for a fixed disk contrast, it becomes easier to discriminate between disk present and disk absent. Ohara *et al.*[34] have derived an equation relating u to the probability of a correct choice, $p(d')$ in an M-alternative choice experiment as:

$$p(d') = \int_{-\infty}^{\infty} [\Phi(t)]^{M-1} \frac{1}{\sqrt{2\pi}} \exp\left(-\frac{(uC-t)^2}{2}\right) dt \quad (15)$$

where $\Phi(t)$ is the cumulative Gaussian distribution. The estimates of u were obtained using a maximum-likelihood method (Appendix B of Ref. 34).

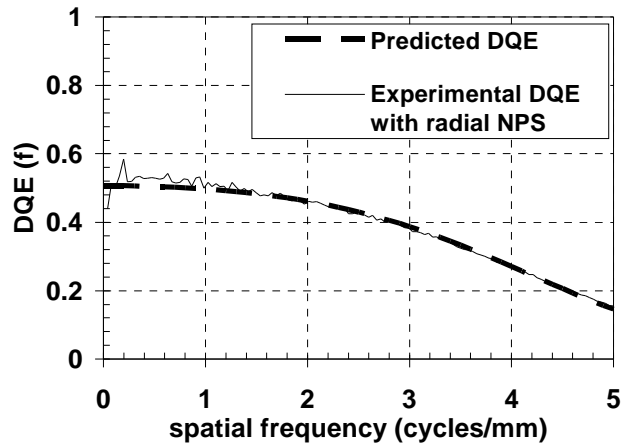
Burgess[33] has described a method for determining the uncertainty in an M-AFC experiment with fixed stimuli. In this study we have K trials defined by N repetitions at L contrast levels ($K = NL$). The response of each trial is binomially distributed. The threshold contrast was defined at 50% and 75% probability of correct response.

4. RESULTS AND DISCUSSION

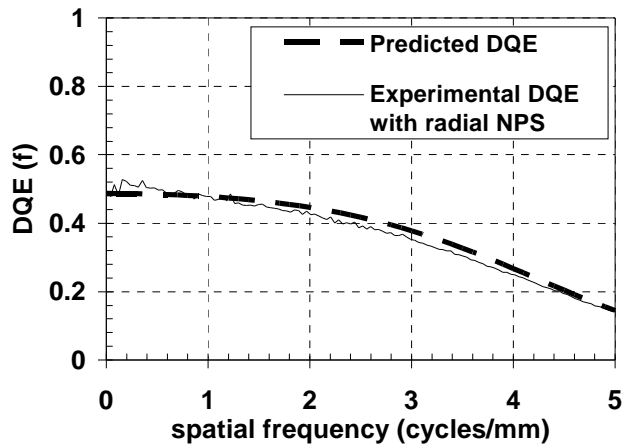
4.1 Predicted Model:

With the serial cascaded systems model presented by Siewerdsen *et al.*[9], a comparison of the theoretical and experimental DQEs calculated using radial NPS has been reported in Figs. 8-10 and a comparison of the theoretical and experimental DQEs calculated using horizontal NPS has been reported in Figs. 11-13. The DQEs from the predicted model matched better to the experimental DQEs calculated with NPS along the horizontal axis than that with NPS along the radial axis. The radial NPS is an average of the two dimensional NPS (that is the radial NPS considers both the vertical and horizontal NPS).

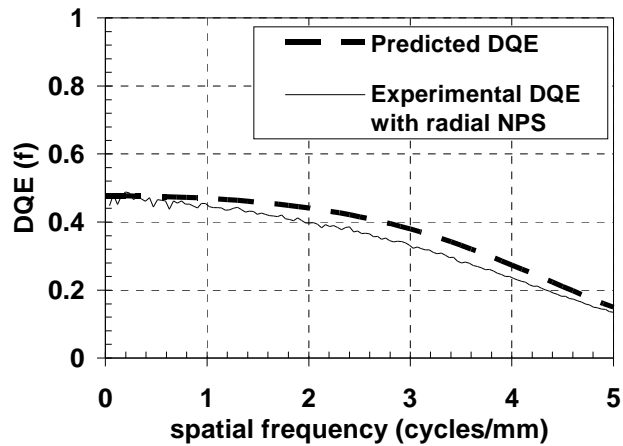
The predicted DQEs may have matched the experimental DQEs (calculated using the horizontal NPS) better because the MTF was measured with the slit positioned in the horizontal direction. The imaging system parameters used in the simulation of the DQE are shown in Table III. The packing efficiency, fill factor and the photons counts per keV were the parameters to be varied to obtain good theoretical fits to the experimental DQE data. The packing efficiency of 70% reported by Cendre *et al.*[35] is used in the predicted model. Antonuk *et al.*[6] have reported a fill factor of 0.5 for AMFPIs incorporating discrete photodiodes. Since the FFDM detector consists of discrete photodiodes, the same fill factor has been assumed. The light output of the CsI:Tl was found to be between 54-56 photons/keV[36]. The DQE decreases with increase in beam-hardening. This decrease depends upon the tradeoffs in quantum detection efficiency, quantum gain, Poisson excess and MTF. As the Lucite thickness



(a)

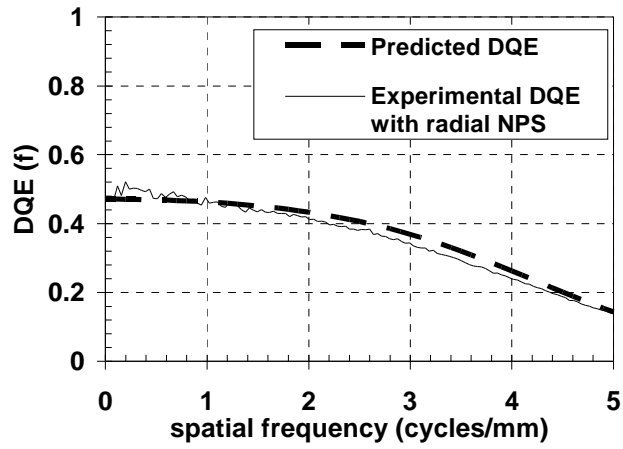


(b)

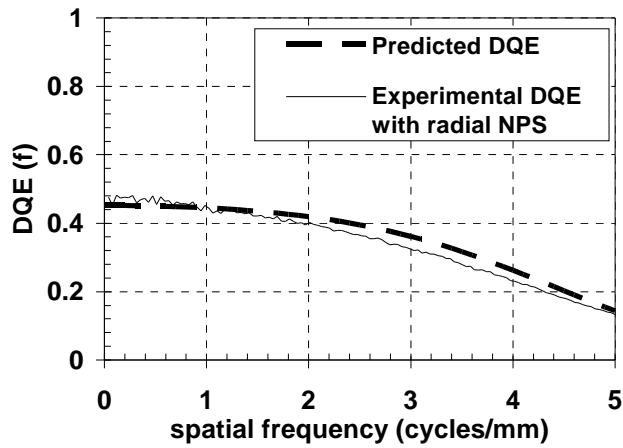


(c)

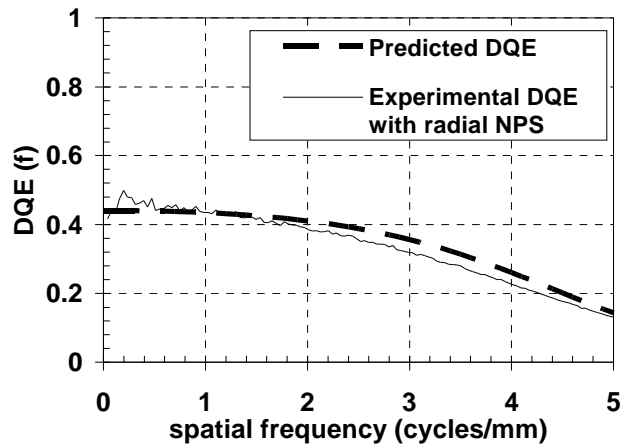
Figure 8: Predicted and experimental DQEs at 26 kVp, Mo/Mo and hardened by 20 mm, 45 mm and 60 mm Lucite are shown in (a), (b) and (c) respectively. The experimental DQEs were calculated using 1D NPS taken along the radial axis. The continuous line represents the experimental DQE and the dashed line represents the predicted DQE.



(a)

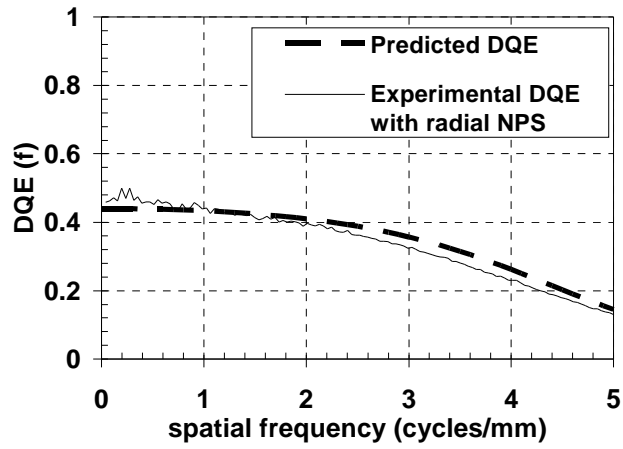


(b)

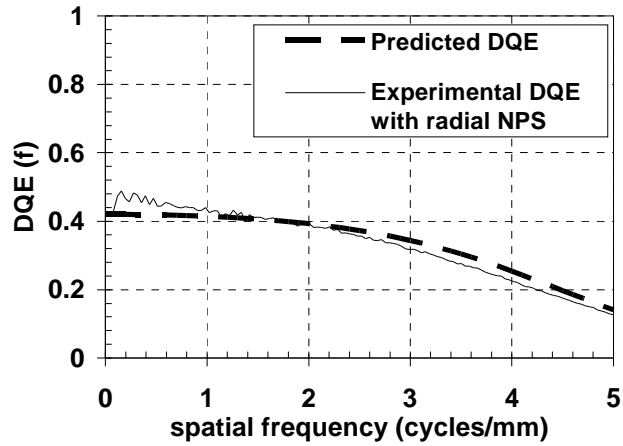


(c)

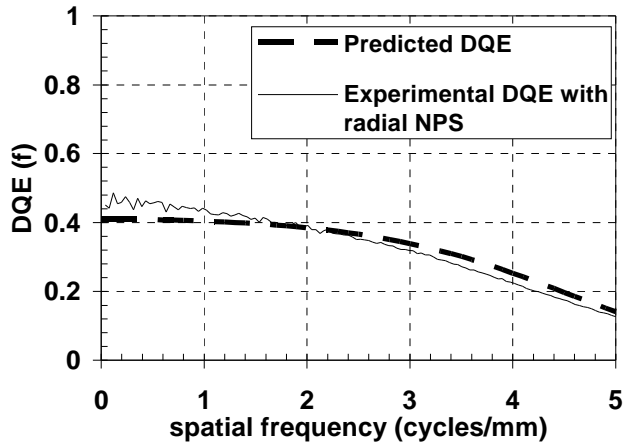
Figure 9: Predicted and experimental DQEs at 28 kVp, Mo/Rh and hardened by 20 mm, 45 mm and 60 mm Lucite are shown in (a), (b) and (c) respectively. The experimental DQEs were calculated using 1D NPS taken along the radial axis. The continuous line represents the experimental DQE and the dashed line represents the predicted DQE.



(a)

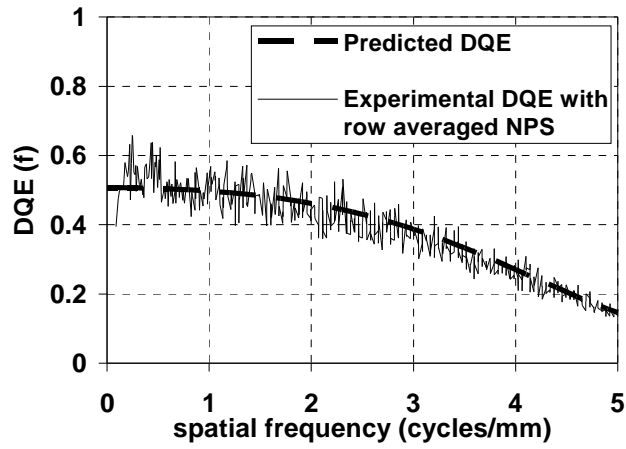


(b)

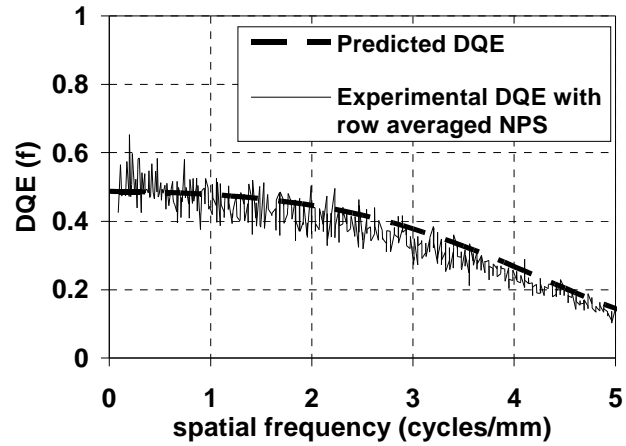


(c)

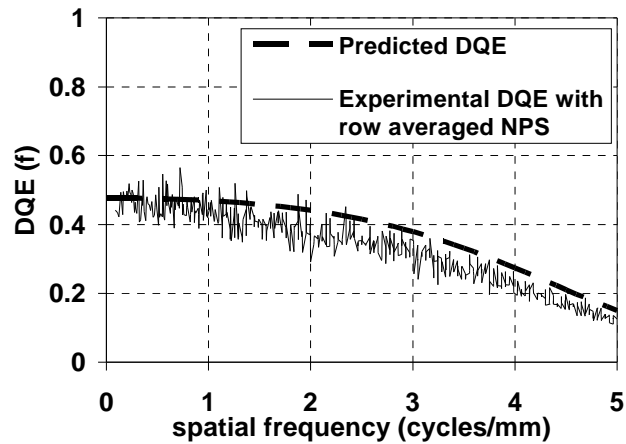
Figure 10: Predicted and experimental DQEs at 30 kVp, Rh/Rh and hardened by 20 mm, 45 mm and 60 mm Lucite are shown in (a), (b) and (c) respectively. The experimental DQEs were calculated using 1D NPS taken along the radial axis. The continuous line represents the experimental DQE and the dashed line represents the predicted DQE.



(a)

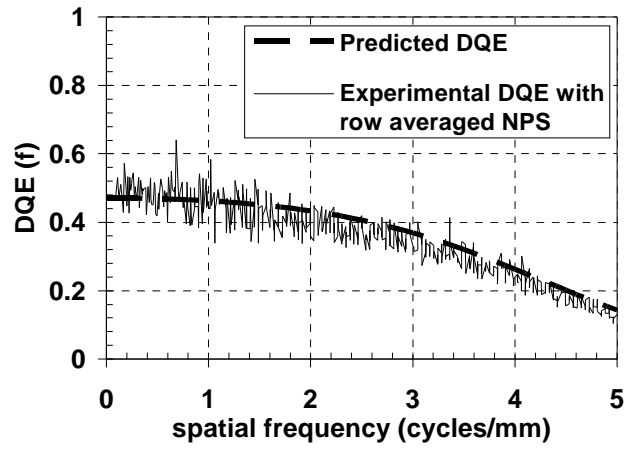


(b)

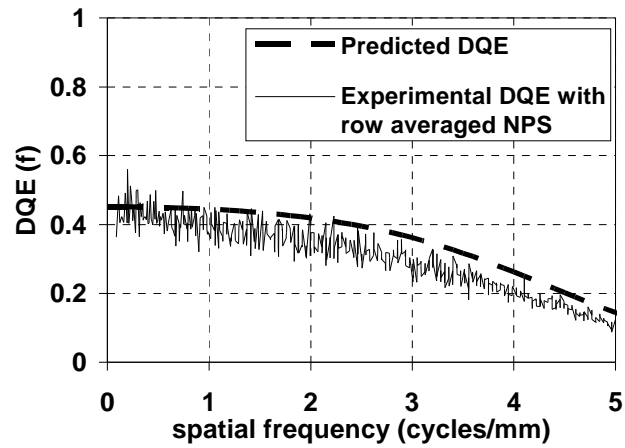


(c)

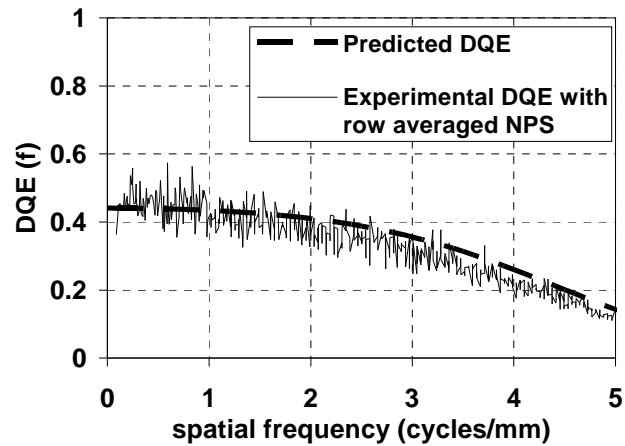
Figure 11: Predicted and experimental DQEs at 26 kVp, Mo/Mo and hardened by 20 mm, 45 mm and 60 mm Lucite are shown in (a), (b) and (c) respectively. The experimental DQEs were calculated using 1D NPS taken along the horizontal axis. The continuous line represents the experimental DQE and the dashed line represents the predicted DQE.



(a)

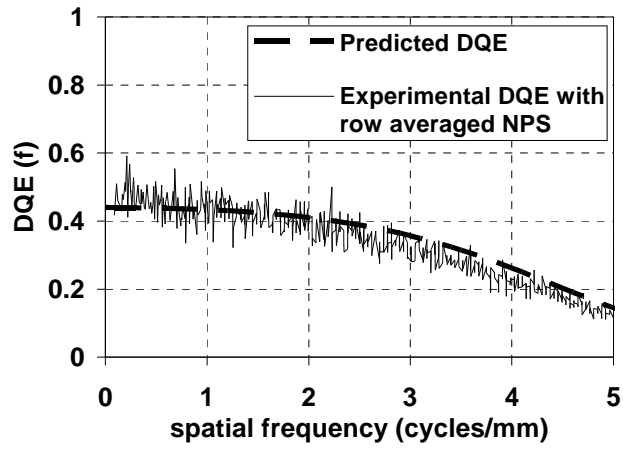


(b)

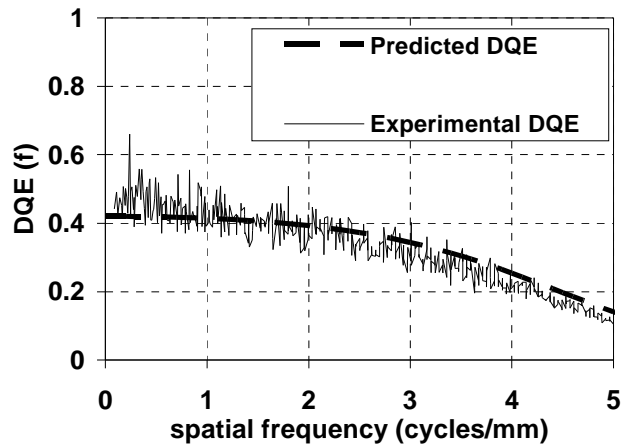


(c)

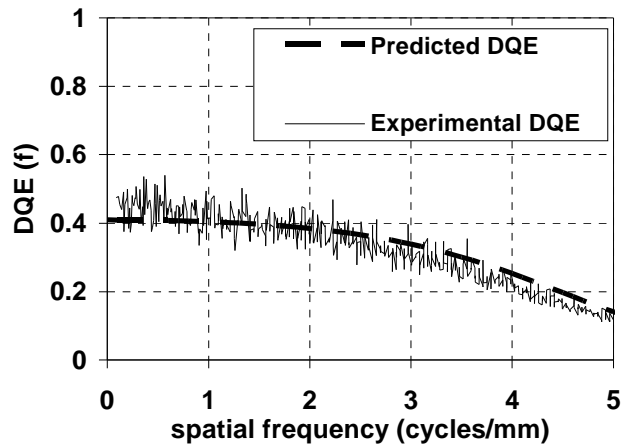
Figure 12: Predicted and experimental DQEs at 28 kVp, Mo/Rh and hardened by 20 mm, 45 mm and 60 mm Lucite are shown in (a), (b) and (c) respectively. The experimental DQEs were calculated using 1D NPS taken along the horizontal axis. The continuous line represents the experimental DQE and the dotted line represents the predicted DQE.



(a)



(b)



(c)

Figure 13: Predicted and experimental DQEs at 30 kVp, Rh/Rh and hardened by 20 mm, 45 mm and 60 mm Lucite are shown in (a), (b) and (c) respectively. The experimental DQEs were calculated using 1D NPS taken along the horizontal axis. The continuous line represents the experimental DQE and the dashed line represents the predicted DQE.

increases, the quantum efficiency, g_1 , decreases and the quantum gain, g_2 , increases keeping the fill factor constant.

Target/Filter	Mo/Mo			Mo/Rh			Rh/Rh		
Lucite thickness (mm)	20	45	60	20	45	60	20	45	60
q_0 (measured)	448055	468995	535989	493158	547577	577541	603438	629189	680762
Exposure (mR)	10.198	9.575	10.391	9.891	9.772	9.828	10.573	9.994	10.365
Transmission factor	0.851	0.869	0.877	0.865	0.886	0.893	0.884	0.900	0.905
a_{pix}	100			100			100		
g_4	0.65			0.65			0.65		
Packing efficiency	0.70			0.70			0.70		
Density of CsI:Tl (g/cm^3)	4.51			4.51			4.51		
W_{CsI} (photons/keV)	54			54			54		
fill factor (f_{pd})	0.5			0.5			0.5		
H parameter	0.115			0.115			0.115		

Table III: Imaging system parameters that were used in the cascaded model for predicting the DQE.

4.1.1 Effects of different system parameters on the DQE:

All the system parameters affect the DQE of the system differently. DQE increased with increase in fill factor, packing efficiency and coupling efficiency, varying only one of the parameters at a time. Increase in packing efficiency, increases the quantum efficiency, g_1 , that increases the DQE. As the fill factor and photon output of the scintillator are increased, the signal per pixel increases, which thus increases the DQE. Studies have shown that there is considerable improvement in the zero frequency DQE (DQE(0)) with increasing fill factor up to ~ 0.5 , above which the DQE(0) improves only marginally[14]. For a system with no additive noise the DQE would be nearly constant in the frequency domain. The DQE falls off rapidly at higher spatial frequency because the shape depends upon the system MTF, the NPS

and the additive noise. From the H-parameter fit for the MTF, it was observed that as H-parameter increases the MTF degrades thus decreasing the DQE at high frequencies. From the model, it can also be noted that increase in the scintillator thickness will increase DQE to a certain level only at lower frequencies while introducing a drop in the MTF ($T_3(u,v)$) of the scintillator. This drop in MTF will initiate a rapid fall-off in the DQE at higher frequencies. An increase in pixel pitch of the scintillator will increase the signal along with the noise to the detector. This will result in an increase in the DQE at lower frequencies, but the higher frequency DQE will suffer. A decrease in DQE, by varying the system parameters, is significant only if the decrease is greater than 3-5 %. The decrease of 2-3 % in the DQE can be attributed to the noise within the system due to variation in system parameters.

4.2 Experimental Data:

The graph shown in Fig.14 represents the presampling MTFs measured without additional Lucite filtration for the three target-filter combinations. Further it was observed that added Lucite filtration produced nearly identical MTFs indicating negligible dependence of MTF characteristics on the energy and type of incident x-ray spectrum.

The simulated and experimentally measured normalized Mo/Mo spectral data are shown in Figs. 15(a-c); the Mo/Rh spectral data are shown in Figs. 16(a-c); and the Rh/Rh spectral data are shown in Figs. 17(a-c). An excellent match between simulated and experimental data of the spectrum was obtained.

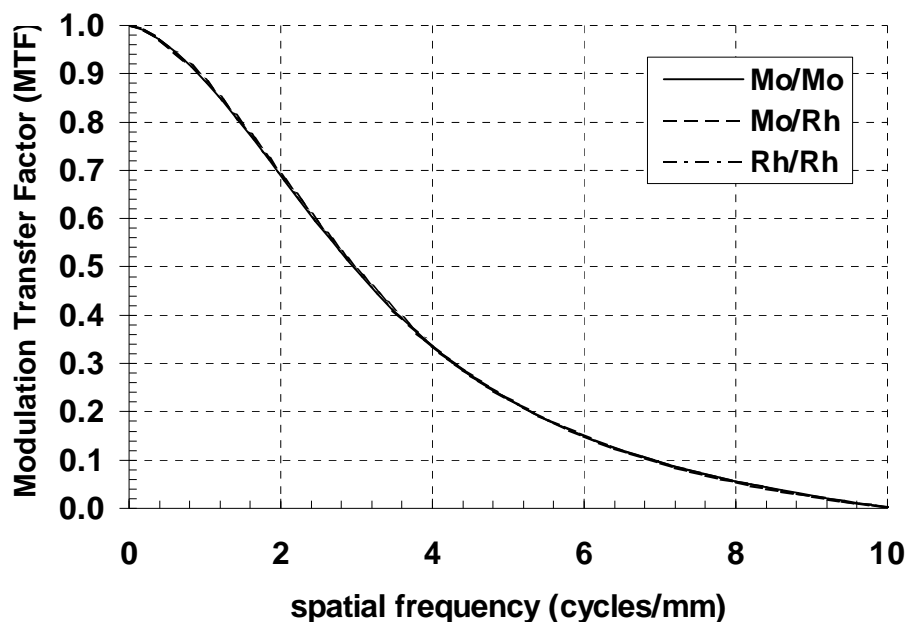
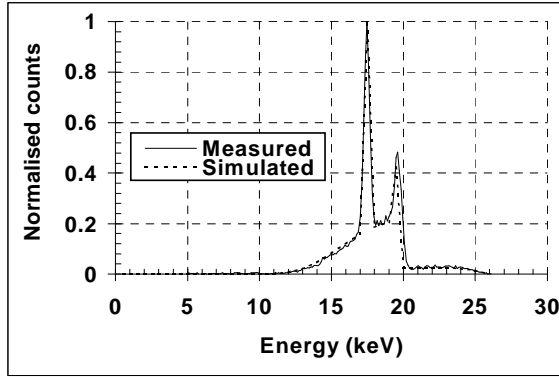


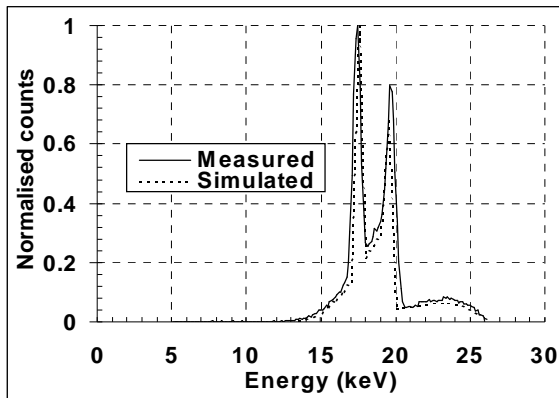
Figure 14: Presampling MTF of the FFDM imager with no added Lucite at different target/filter combinations. Nearly identical MTFs are observed indicating negligible dependence of MTF characteristics on the energy and type of incident x-ray spectrum.

The peak mismatch between the simulated and experimental spectral data in a few cases is due to the finite energy bin of 0.5 keV in the lower energy portion of the spectra followed by a reduction in simulated spectra. The beam hardening effects, due to additional Lucite filtration, result in a reduction the peak-to-peak difference. There was virtually no difference in the measured spectral shape with or without the grid for a given tube voltage and Lucite filtration, as most of the scatter is eliminated by the spectrometer's aperture.

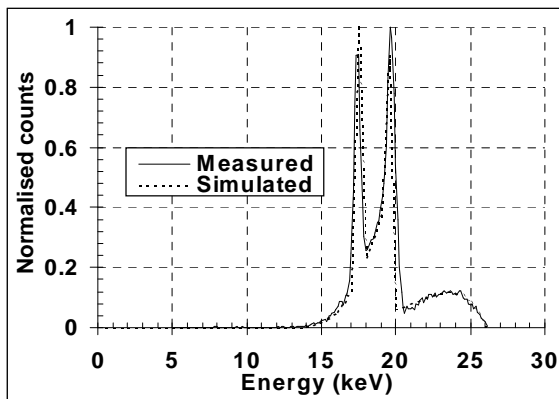
The NPS_{raw} data for the Mo/Mo spectra at various Lucite thicknesses are shown in Fig. 18. In order to maintain the identical incident exposures at various beam-hardening conditions, mAs was increased.



(a)

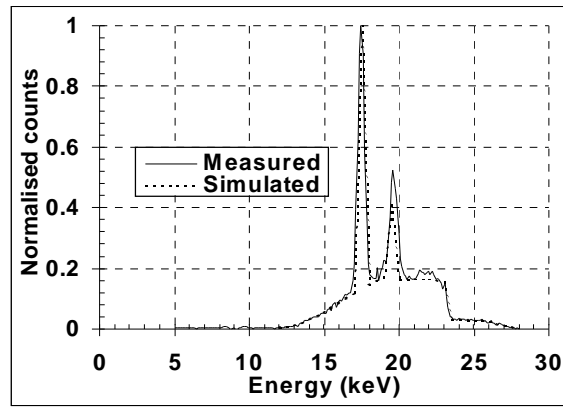


(b)

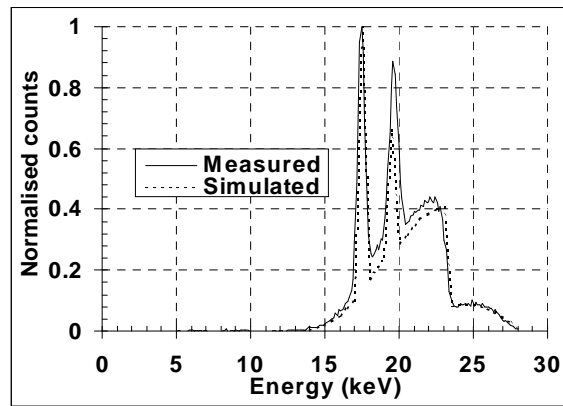


(c)

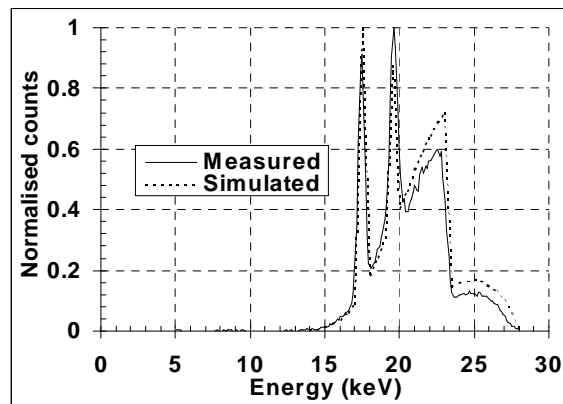
Figure 15: The simulated and measured Mo/Mo spectra obtained at 26 kVp and transmitted through 20 mm, 45 mm and 60 mm Lucite are shown in (a), (b) and (c) respectively. The continuous line represents the measured spectra and the dashed line represents the simulated spectra. The measured and simulated spectra match well.



(a)

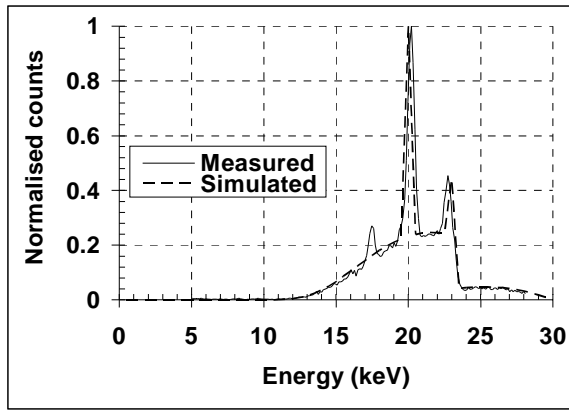


(b)

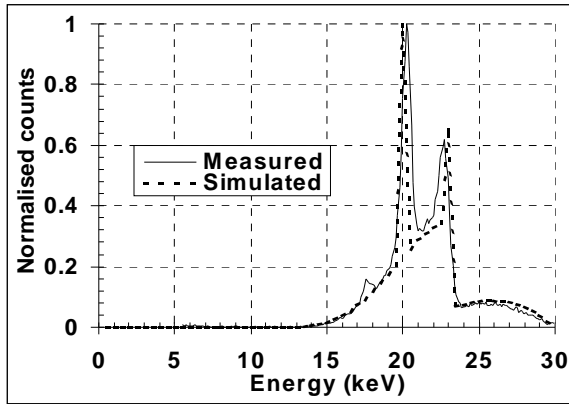


(c)

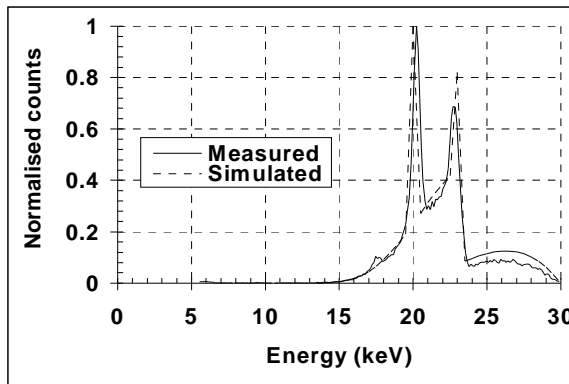
Figure 16: The simulated and measured Mo/Rh spectra obtained at 28 kVp and transmitted through 20 mm, 45 mm and 60 mm Lucite are shown in (a), (b) and (c) respectively. The continuous line represents the measured spectra and the dashed line represents the simulated spectra. The measured and simulated spectra match well.



(a)



(b)



(c)

Figure 17: The simulated and measured Rh/Rh spectra obtained at 30 kVp and transmitted through 20 mm, 45 mm and 60 mm Lucite are shown in (a), (b) and (c) respectively. The continuous line represents the measured spectra and the dashed line represents the simulated spectra. The measured and simulated spectra match well.

The increase in NPS_{raw} can be attributed to the increase in the number of incident x-ray photons that directly contribute to x-ray photon noise in a quantum noise limited system. It has been shown by many authors that the incident photons/mm²/mR increase with x-ray filtration in mammography[27] at a given exposure level. Similar results were observed with the Mo/Rh and Rh/Rh spectral combinations. The $NPS_{\text{normalized}}$ characteristics for the Mo/Mo spectra with additional Lucite filtration are shown in Fig. 19. A lower noise level was observed with 6 cm Lucite filtration mainly due to an increase in the average signal value. Similar trends were observed with Mo/Rh and Rh/Rh spectral data.

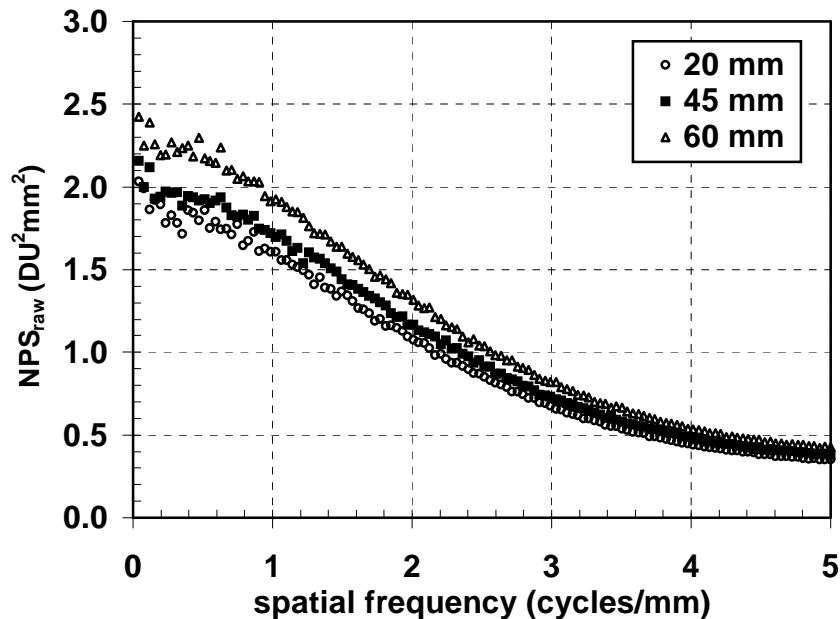


Figure 18: Raw NPS of the system measured at 26 kVp, Mo/Mo and hardened by different thickness of Lucite. An incident exposure of approximately 10 mR was maintained at the detector. Noise increases with increase in Lucite thickness. Similar trends were observed with Mo/Rh and Rh/Rh at different beam hardening conditions.

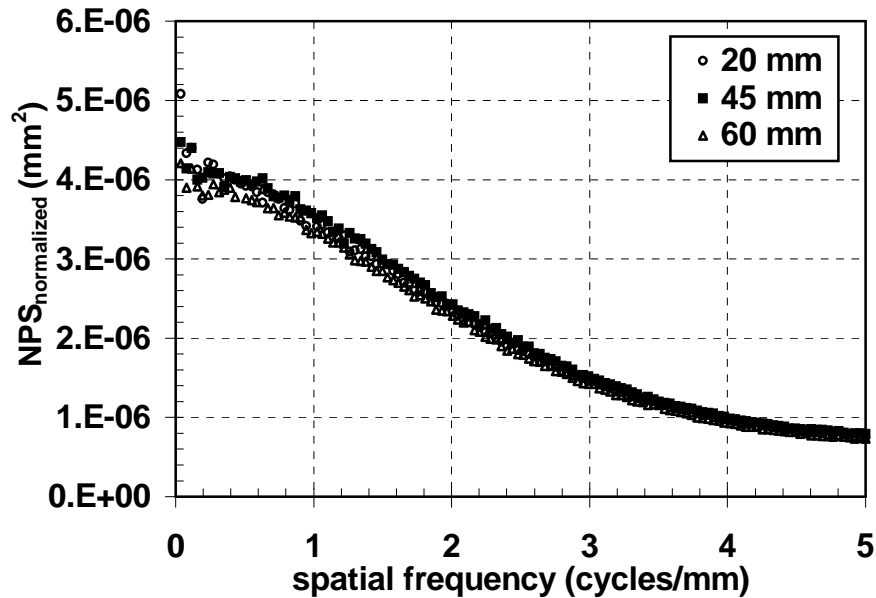


Figure 19: Normalized NPS of the system measured at 26 kVp, Mo/Mo and hardened by different thickness of Lucite. An incident exposure of approximately 10 mR was maintained at the detector. Normalized noise decreases with increase in Lucite thickness because the mean signal value increases. Similar trends were observed with Mo/Rh and Rh/Rh at different beam hardening conditions.

The DQE(f) characteristics of the digital mammography system with Mo/Mo spectra and additional Lucite filtration is shown in Fig. 21. A decreasing trend in the DQE(f) with increased Lucite filtration was observed and it agrees with a recent data reported by Tkaczyk *et al.*[27]. Relatively higher DQE(f) characteristics were observed with Mo/Mo followed by Mo/Rh and Rh/Rh. The decrease in the DQE can be ascribed to a combination of an increase in the incident quanta 'q' with a decrease in the quantum detection efficiency of the CsI:Tl scintillator at higher energy levels. The decrease in quantum detection efficiency with increase in Lucite thickness is shown in Fig. 20. The proportional increase in the average signal level (digital units) was also relatively lower compared to the increase in the incident quanta contributing to a decrease in the DQE(f) of the system. We observed similar results with Mo/Rh and Rh/Rh DQE(f) data (Figs. 22, 23).

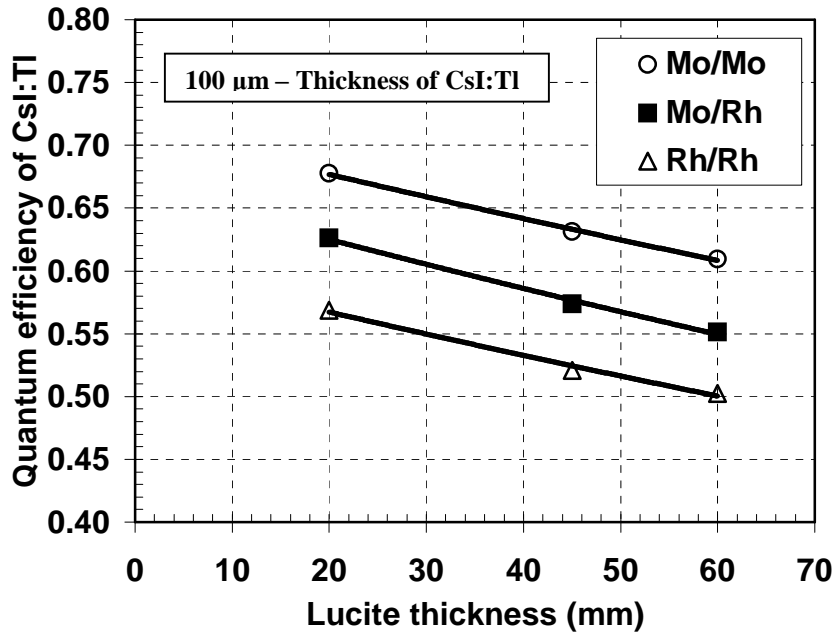


Figure 20: Quantum detection efficiency of a 100 μm thick CsI:Tl scintillator for all target/filter combinations. The decrease in efficiency causes a decrease in DQE of the system at higher energy levels. Exponential trend lines fit to the data show the exponential nature of the quantum efficiency of CsI:Tl.

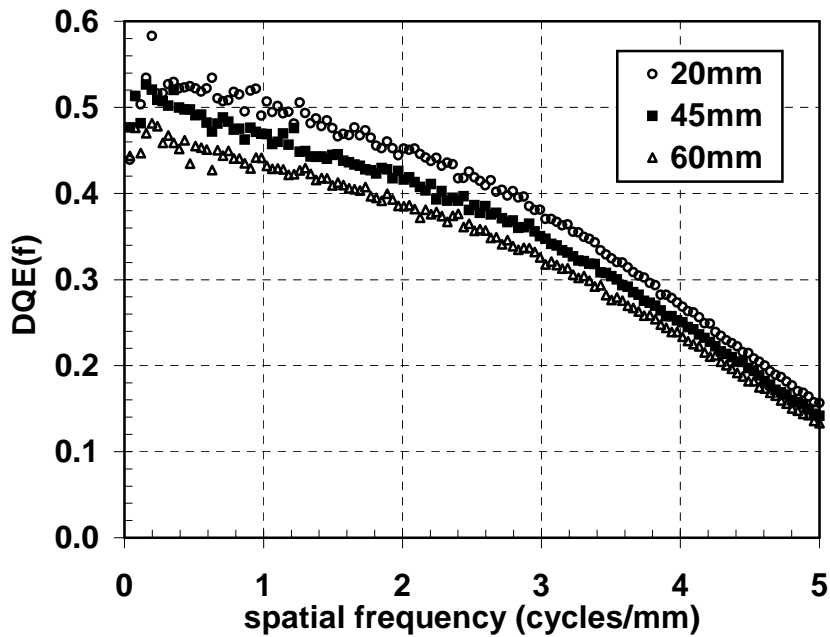


Figure 21: DQE of the system measured at 26 kVp, Mo/Mo and hardened by different thickness of Lucite. An incident exposure of approximately 10 mR was maintained at the detector.

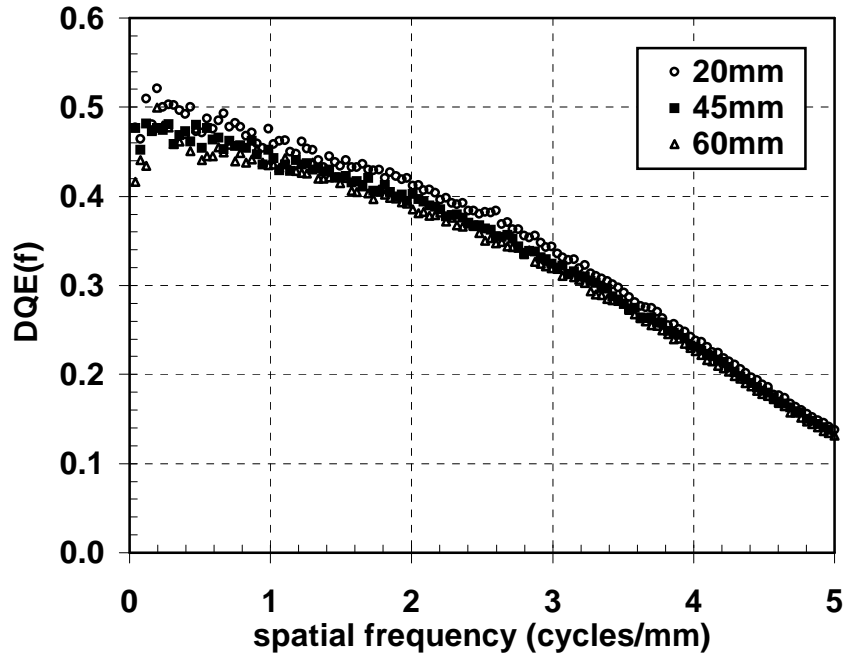


Figure 22: DQE of the system measured at 28 kVp, Mo/Rh and hardened by different thickness of Lucite. An incident exposure of approximately 10 mR was maintained at the detector.

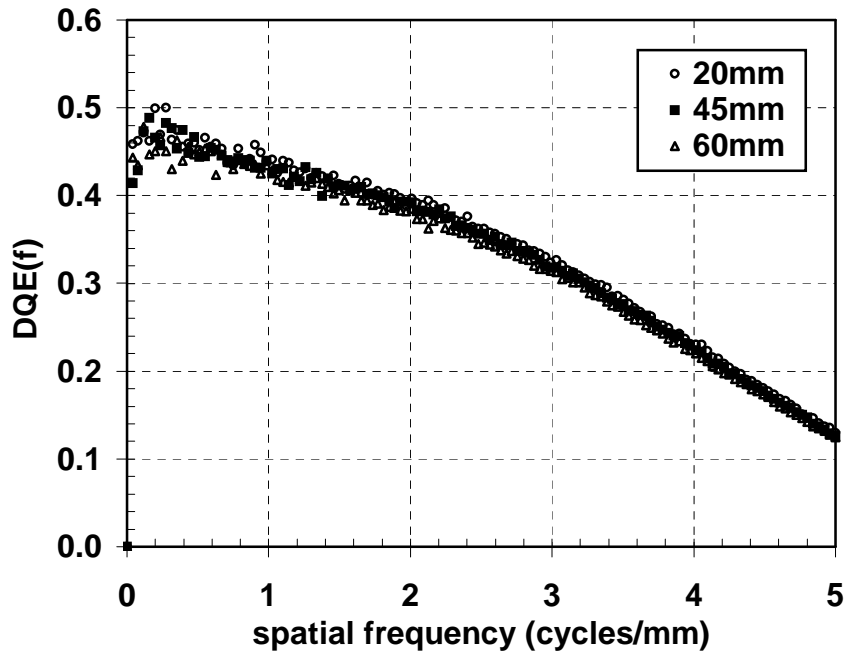


Figure 23: DQE of the system measured at 30 kVp, Rh/Rh and hardened by different thickness of Lucite. An incident exposure of approximately 10 mR was maintained at the detector.

Reduced NPS_{raw} due to the use of anti-scatter grid is shown in Fig. 24. The anti-scatter grid decreases the average signal level that in turn causes an increase in the normalized noise levels with the anti-scatter grid when compared to those without the grid (Fig. 25). The DQE(f) characteristics for all the three target-filter combinations with 45 mm Lucite filtration are shown in Figs. 26-28. A noticeable drop in the DQE(f) is obtained if the anti-scatter grid is considered to be an integral part of the clinical system and 'pre-grid' exposure values are used when computing DQE. On the contrary, the grid cuts off a significant portion of the incident exposure reducing it by nearly half the 'pre-grid' exposure, thereby exposing the detecting medium to only half the incident exposure past the anti-scatter grid. The DQE(f)s measured without the grid for all three target-filter combinations were lower as compared to the DQE(f)s that resulted from the use of post-grid exposure values.

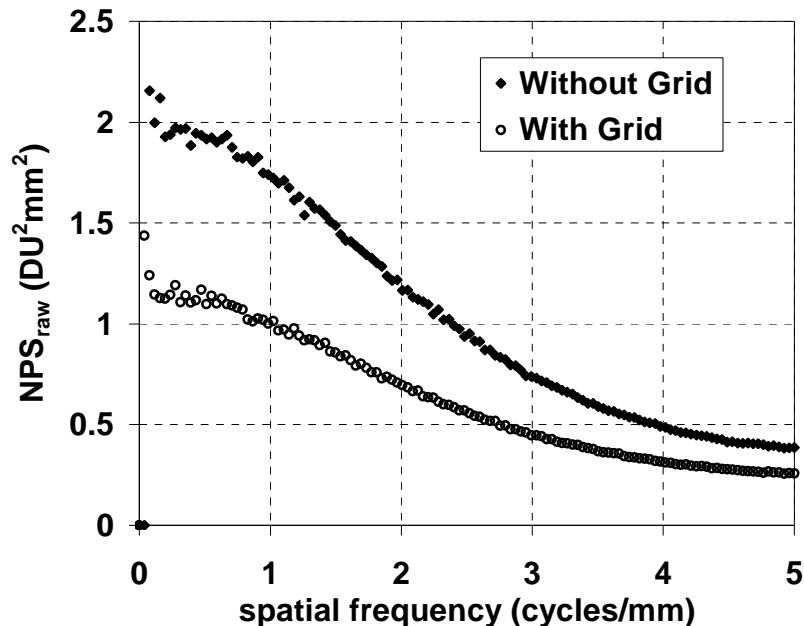


Figure 24: Raw NPS measured at 26 kVp, Mo/Mo with 45 mm of Lucite and a 'pre-grid' exposure of approximately 10 mR. Noise decreases with the anti-scatter grid in place. Similar trends are observed with Mo/Rh and Rh/Rh target/filter combinations.

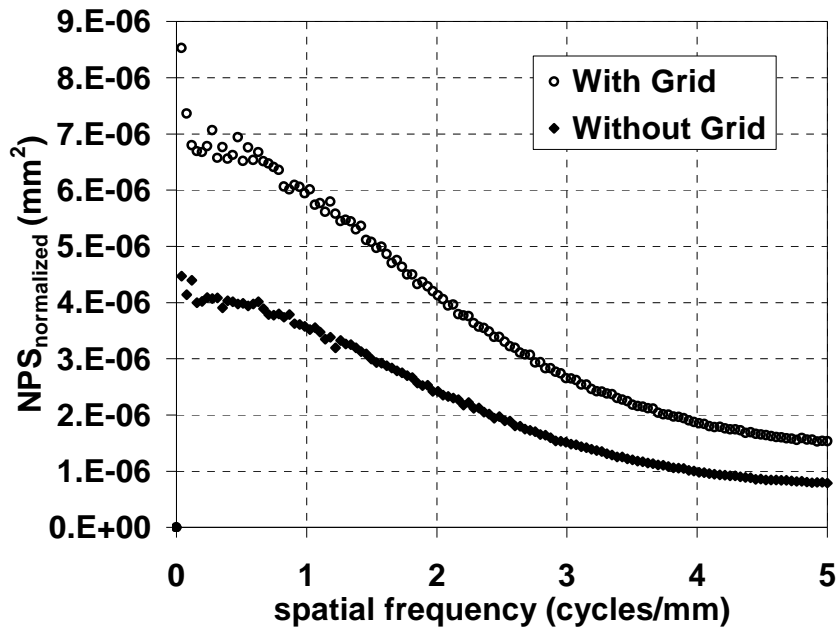


Figure 25: Normalized NPS measured at 26 kVp, Mo/Mo with 45 mm of Lucite and a 'pre-grid' exposure of approximately 10 mR. Normalized noise increases with the anti-scatter grid in place due to decrease in the average signal. Similar trends are observed with Mo/Rh and Rh/Rh target/filter combinations.

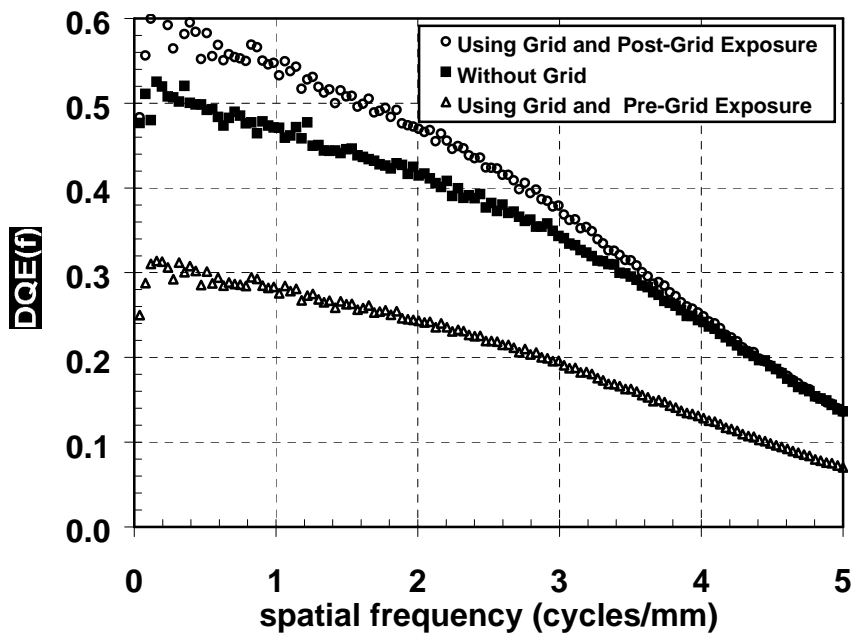


Figure 26: DQE of the system measured at 26 kVp, Mo/Mo and hardened by using 45 mm Lucite. The measured exposure without the grid was 9.575 mR while the post grid exposure was 4.915 mR.

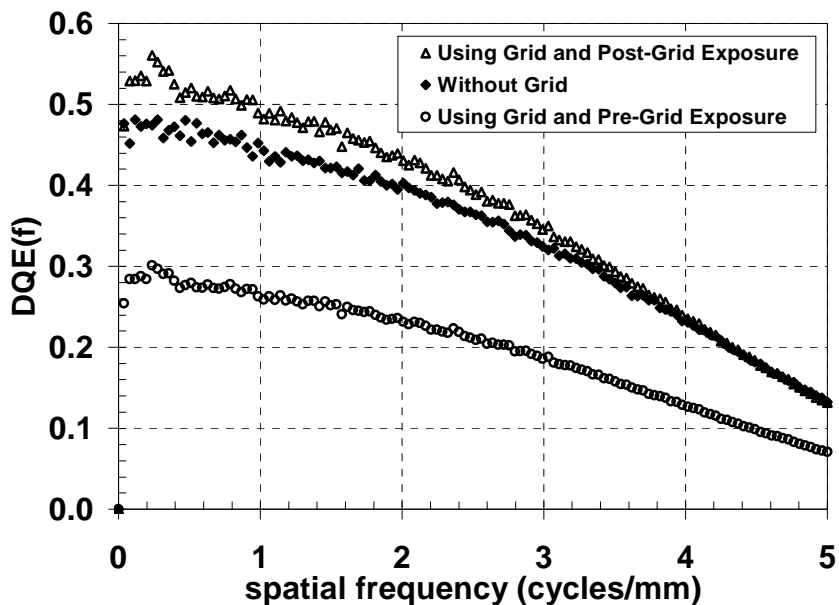


Figure 27: DQE of the system measured at 28 kVp, Mo/Rh and hardened by using 45 mm Lucite. The measured exposure without the grid was 9.772 mR while the post grid exposure was 5.264 mR.

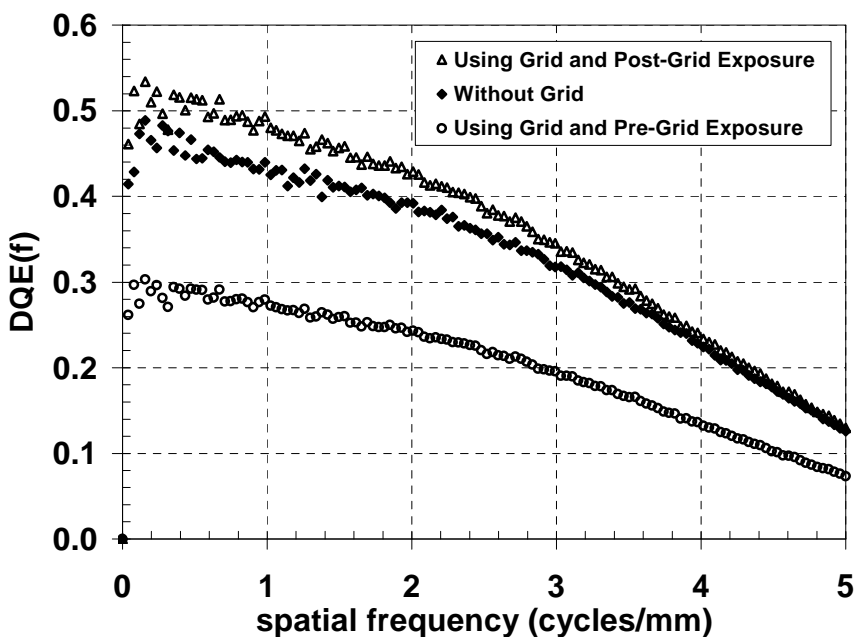


Figure 28: DQE of the system measured at 30 kVp, Rh/Rh and hardened by using 45 mm Lucite. The measured exposure without the grid was 9.994 mR while the post grid exposure was 5.585 mR.

A $DQE(0)$ in the range of 0.45 to 0.50 was obtained for various x-ray beam hardening and target-filter combinations without the anti-scatter grid. The $DQE(0)$ s that were measured with the anti-scatter grid ranged from 0.30 to 0.58 depending on the incident exposure condition that was used for DQE computations. The $DQE(f)$ characteristics with the anti-scatter grid are much lower compared to the $DQE(f)$ s measured without using the grid in all the cases, even when using a post-grid incident exposure close to 10 mR (Figs. 29-31). We obtained $DQE(0)$ values in the range of 0.27-0.30 with the anti-scatter grid and post-grid exposures close to 10 mR on the detector. Although the noise levels reduced due to anti-scatter grid, the average signal level was also reduced, which caused an increase in $NPS_{normalized}$ thereby reducing the DQE.

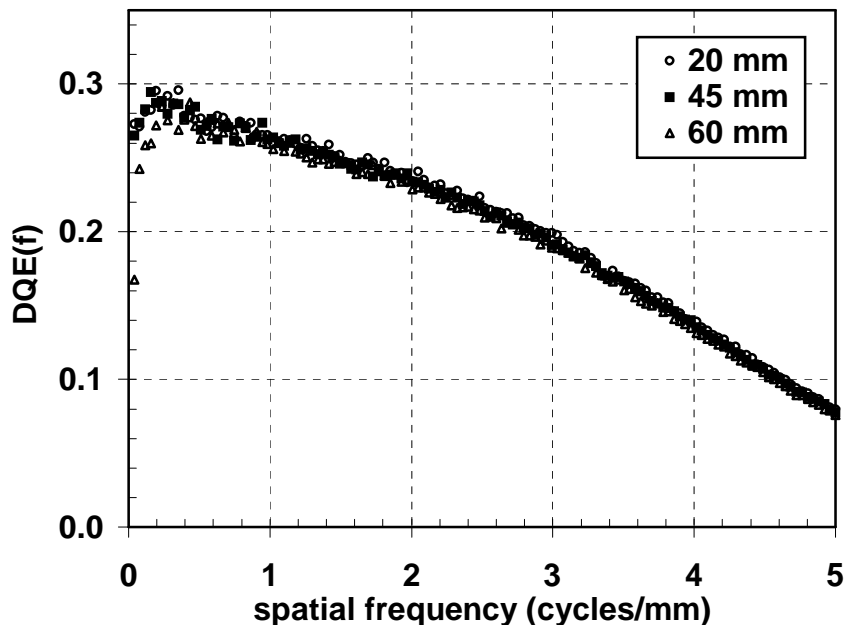


Figure 29: DQE of the system measured at 26 kVp, Mo/Mo with anti-scatter grid and hardened by varying the thickness of Lucite. A post-grid exposure of approximately 10 mR was maintained on the detector.

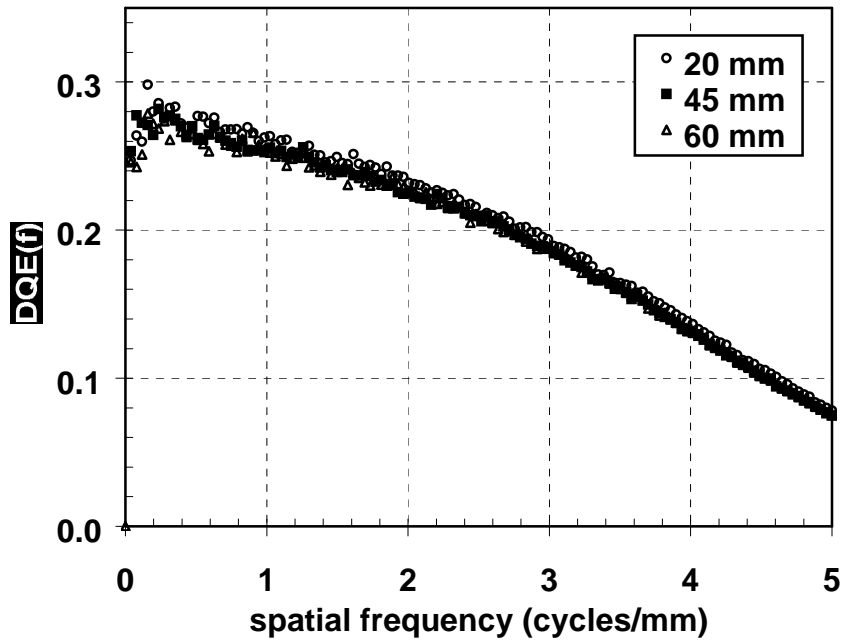


Figure 30: DQE of the system measured at 28 kVp, Mo/Rh with anti-scatter grid and hardened by varying the thickness of Lucite. A post-grid exposure of approximately 10 mR was maintained on the detector.

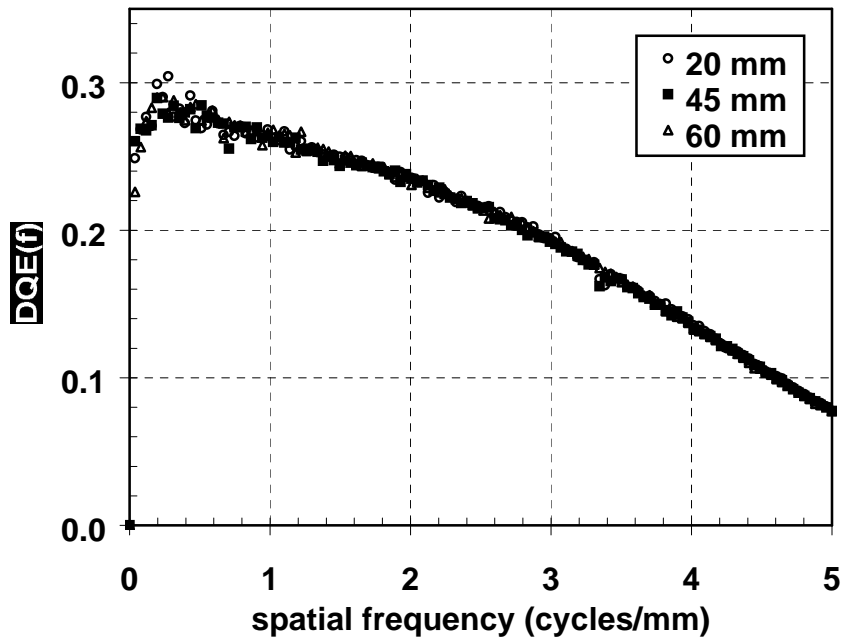


Figure 31: DQE of the system measured at 30 kVp, Rh/Rh with anti-scatter grid and hardened by varying the thickness of Lucite. A post-grid exposure of approximately 10 mR was maintained on the detector.

4.3 Contrast-detail study:

Percent correct detection curve generated using MLE technique for a single observer for a disk diameter of 0.80 mm is shown in Fig. 32. The errors due to the u-parameter estimation are indicated as dotted lines in the graph.

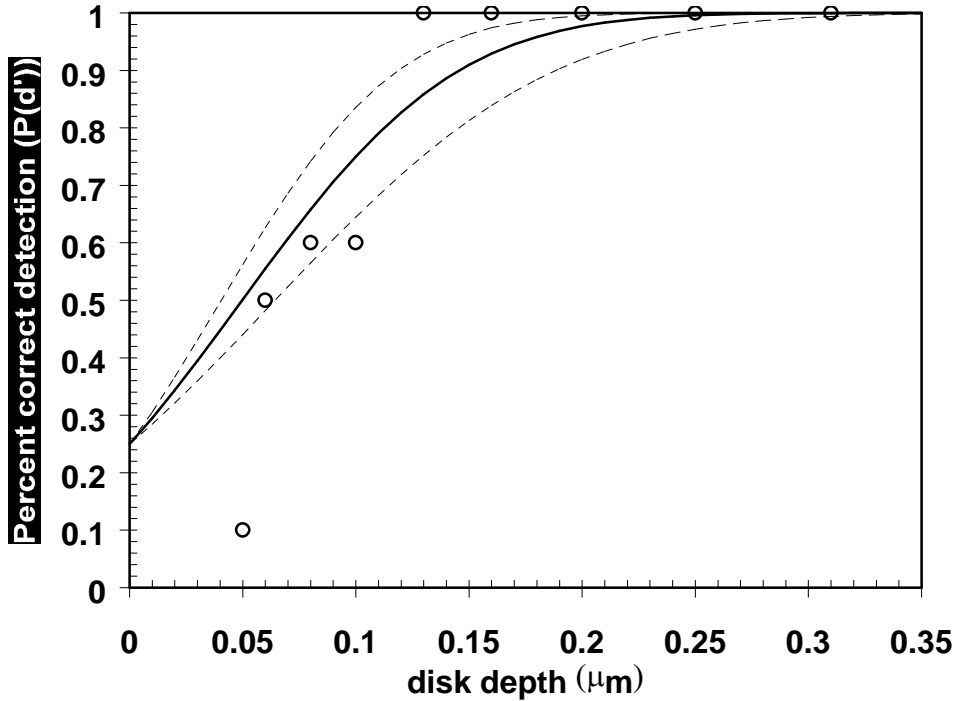


Figure 32: Percent correct detection characteristics of a single observer are shown for the uncompressed images at 0.80 mm disk diameter. The markers represent experimental data points and the smooth lines represent estimated detection characteristics obtained by the maximum likelihood estimation (MLE) fit. Similar curves were obtained for all observers at different disk diameters.

A comparison of the percent correct detection data for a single observer corresponding to disk diameters 0.80 mm for the uncompressed and compressed images is as shown (Fig. 33). It is apparent from the results that the uncompressed images exhibit comparatively better “percent correct” characteristics (steeper slope) compared to the compressed images.

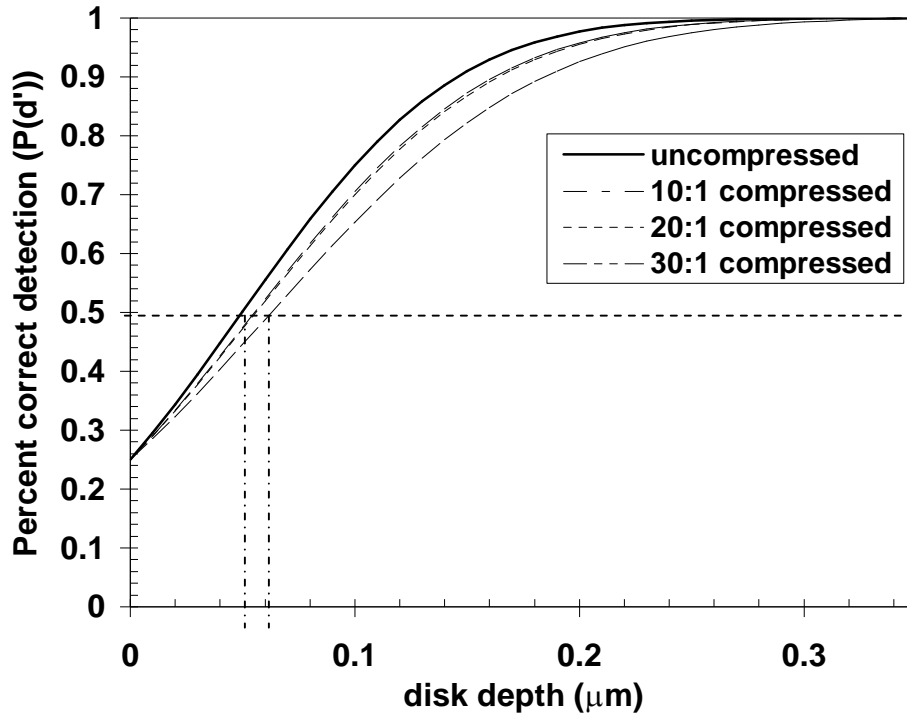


Figure 33: Percent correct detection characteristics for a single observer are shown for the uncompressed images for disk diameter of 0.80 mm. The horizontal dashed line represents a 50% threshold level. The projection of the vertical dashed-dotted lines on the x-axis gives the disk depths corresponding to the disk diameters, thus generating CD characteristics. Similarly, CD characteristics were obtained for all the observers for all the uncompressed and compressed images at 75% threshold level.

The contrast detail characteristics for the uncompressed and the compressed phantom images at 50% and 75% threshold levels are shown in Figs. 34 and 35 respectively. Although lower (better) contrast characteristics were observed for the uncompressed images, there was no significant difference of contrast characteristics of 10:1 compressed images at smaller disk diameters for both the threshold levels. Compression altered the detectability of disks only at larger disk diameters, for uncompressed and 10:1 compressed images. The threshold contrast characteristics for the 20:1 compressed images matched approximately to those for 30:1 compressed

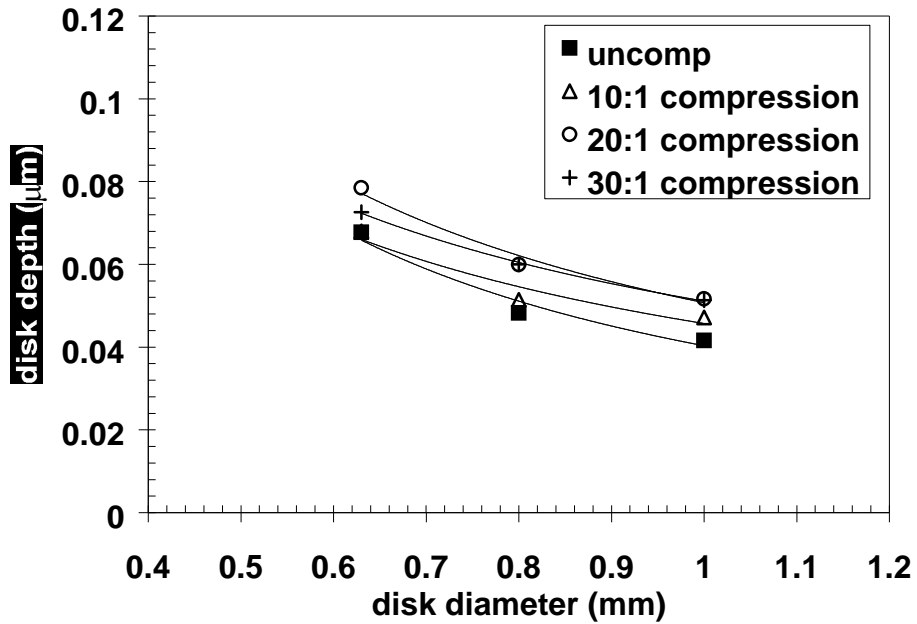


Figure 34: Mean CD characteristics obtained at 50% threshold level for all the uncompressed and compressed images. The different lines indicate model predicted CD diagrams for the uncompressed and compressed images.

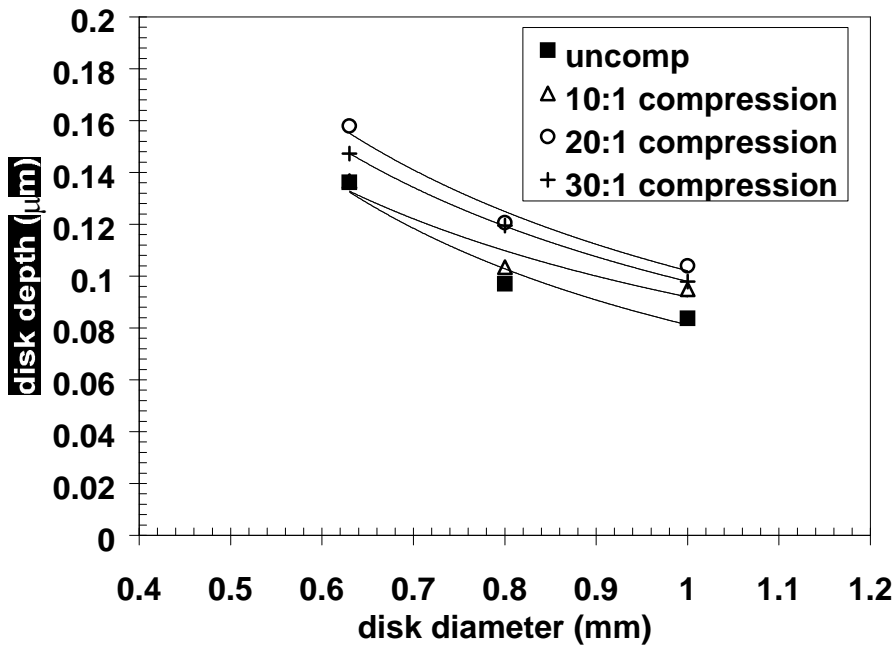


Figure 35: Mean CD characteristics obtained at 75% threshold level for all the uncompressed and compressed images. The different lines indicate model predicted CD diagrams for the uncompressed and compressed images.

images as the disk diameter increased. The 20:1 compressed images had the highest (poor) contrast characteristics at smaller disk diameters when CD characteristics of uncompressed and all compressed images were compared.

Compression causes the image to smoothen and, therefore, the observers could detect the location of the corner disk in 30:1 compressed images more easily for all disk depths resulting in lower (better) contrast detail characteristics compared to that for 20:1 compressed images. Similar contrast characteristics, at smaller disk diameters, for uncompressed and 10:1 compressed images can be attributed to the fact that low compression ratios do not affect the human detectability of small objects.

The contrast-detail methodology is widely used for the evaluation of clinical imaging system. Psychological measurements using alternative forced choice (AFC) methods with phantom images have been widely studied[22,23,33,34,37]. AFC techniques are convenient means to compare modalities rather than measuring their absolute detectability. Since the phantom has many disks, it makes it difficult for the observer to memorize the signal locations. The randomized signal location further alleviates observer learning to a great extent. The AFC methods also provide an opportunity to evaluate the CD characteristics at multiple threshold levels, which is not possible with conventional CD experiments.

5. CONCLUSION

A powerful incentive for the development of the theoretical models describing the signal and noise properties of imagers is to allow an examination of the potential performance of hypothetical systems. The generality of the theoretical cascaded model approach provides not only a means of predicting and optimizing the performance of a given system, but it also provides an objective means of comparing the potential performance of existing systems. The DQEs obtained from the predicted model matched the experimental data very well and thus it can be concluded that further studies should be conducted where cascaded models can be tested to predict reliable DQEs for combinations of various beam-hardening and other parameters for system optimization. In aSi:H imagers, there is a necessary tradeoff between pixel pitch and fill factor for the matrix array with a discrete photodiode design. Matrix arrays incorporating a continuous photodiode design, can be a solution to this problem[38]. Linear cascaded systems modeling provides a tool for exploring imager optimization by examining the effects of varying system parameters on the DQE. An imager configuration that maximizes DQE for a given set of exposure conditions can be determined by exploring the system parameters in an iterative manner. This allows one to estimate the performance of an imager configuration before spending time and expensive resources to develop an imaging system.

A comprehensive characterization of the physical quality parameters such as the detective quantum efficiency of the FFDM system was performed in this study. The effects of x-ray beam hardening, target-filter combinations, and the anti-scatter grid

on the DQE were explored. The DQEs of the FFDM under the various conditions were higher than those reported for mammography screen-film systems[39]. Spectral and system design conditions play a key role in determining the physical quality parameters and hence it is important to take these factors into account when designing a clinical mammography system.

For any clinical mammography examination, the anti-scatter grid is always placed above the detector but the effect of the grid was traditionally ignored in the measurement of the DQE. A DQE of 0.30 was obtained with the anti-scatter grid in place, versus a DQE of 0.50 without the grid. Thus, there is an over estimation of the DQE of the system. Investigators should take a close look at the grid parameters and its effects on the DQE to improve the DQE of the system with the anti-scatter grid. As mentioned before, the DQE obtained for a screen-film mammography system is 0.30 without the anti-scatter grid. The DQE will be lower if measured with the grid in place. Other techniques should be explored to suppress the noise in the incident x-ray beam to the detector.

From the contrast-detail study done with the CDMAM phantom, it can be concluded that on an average, the uncompressed images exhibit lower (better) threshold contrast characteristics compared to the compressed images. The study also shows that the digital images can be compressed to a certain limit with insignificant effect on the detection characteristics. The study mainly demonstrated a technique for CD analysis. Investigations to evaluate the perceptual limit for medical image compression have

been reported[18]. The efficiency of compression depends on the nature of the medical image and the type of task for which the image will be used. Hence anatomical images must be studied with different compression techniques to determine the best technique and compression limit for the particular type of anatomical images.

Although final evaluation of new imaging systems should only be made with clinical images, contrast-detail studies contribute valuable insight into the design and understanding of new systems in addition to being an effective quality assurance tool for comparing various imaging technologies.

6. REFERENCES

1. R. M. Nishikawa, G. E. Mawdsley, A. Fenster and M. J. Yaffe, "Scanned-projection digital mammography," *Med. Phy.* 14(5), 717-727 (1987).
2. R. D. Rosenberg, J. F. Lando, W. C. Hunt et al. , "New Mexico project: screening mammography performance in Albuquerque, New Mexico 1991-1993," *Radiology* 202:591 (1997).
3. M. A. Anastasio, H. Yoshida, R. Nagel, R. M. Nishikawa, and K. Doi, "A genetic algorithm-based method for optimizing the performance of a computer-aided diagnosis scheme for detection of clustered microcalcifications in mammograms," *Med. Phy.* 25, 1613-1620 (1998).
4. M. Kallergi, G. M. Carney, and J. Gaviria, "Evaluating the performance of detection algorithms in digital mammography," *Med. Phy.* 26, 267-275 (1999).
5. J. M. Lewin, E. R. Hendrick, C. J. D'Orsi, P. K. Issacs, L. J. Moss, A. Karellas, G. A. Sisney, C. C. Kuni, and G. R. Cutter, "Comparison of full-field digital mammography with screen-film mammography for cancer detection: results of 4,945 paired examinations," *Radiology* 218, 873-880 (2001).
6. L. E. Antonuk, K. W. Jee, Y. El-Mohri, M. Maolinbay, S. Nassif, X. Rong, Q. Zhao, J. H. Siewerdsen, R. A. Street, and K. S. Shah, "Strategies to improve the signal and noise performance of active matrix, flat-panel imager for diagnostic x-ray applications," *Med. Phy.* 27, 289-306 (2000).
7. J. A. Rowlands and D. M. Hunter, "X-ray imaging using amorphous selenium: A photoinduced charge readout method for digital mammography," *Med. Phy.* 18, 421-431 (1991).

8. Z. Jing, W. Huda, and J. K. Walker, "Scattered radiation in scanning slot mammography," *Med. Phy.* 25, 1111-1117 (1998).
9. J. H. Siewerdsen, L. E. Antonuk, Y. El-Mohri, J. Yorkston, W. Huang, and J. M. Boudry, "Empirical and theoretical investigation of the noise performance of direct detection, active matrix flat-panel imagers (AMFPIs) in diagnostic radiology," *Med. Phy.* 24(1), 71-88 (1997).
10. J. Chabbal, C. Chaussat, T. Ducourant, L. Fritsch, J. Michailos, V. Spinnler, G. Vieux, M. Arques, G. Hahm, M. Hoheizel, H. Horbachek, R. Schulz, and M. Spahn, "Amorphous silicon x-ray image sensor," *Proc. SPIE* 2708, 499-510 (1996).
11. W. Zhao, and J. A. Rowlands, "X-ray imaging using amorphous selenium: Feasibility of a flat panel self-scanned detector digital radiology," *Med. Phy.* 22, 1595-1604 (1995).
12. S. Vedantham, A. Karellas, and S. Suryanarayanan, "Full breast digital mammography with an amorphous silicon-based flat panel detector: Physical characteristics of a clinical prototype," *Med. Phy.* 27 (3), 558-567 (2000).
13. S. Vedantham, A. Karellas, S. Suryanarayanan, C. J. D'Orsi, and R. E. Hendrick, "Breast imaging using an amorphous silicon based full-field digital mammography system: stability of a clinical prototype," *J. Digi. Imaging* 13, 191-199 (2000).
14. J. H. Siewerdsen, "Signal, Noise and Detective Quantum Efficiency of a-Si:H Flat Panel Imagers," PhD Thesis, University of Michigan, Ann Arbor, MI (1998).

15. H. P. Chan, C. J. Vyborny, H. MacMahon, C. E. Metz, K. Doi, and E. A. Sickles, "Digital mammography: ROC studies of the effects of pixel size and unsharp-mask filtering on the detection of subtle microcalcifications," *Invest. Radiol.* 22, 581-589 (1987).
16. H. P. Chan, L. T. Niklason, D. M. Ikeda, K. L. Lam, and D. D. Adler, "Digitization requirements in mammography: Effects on computer-aided detection of microcalcifications," *Med. Phys.* 21, 1203-1211 (1994).
17. B. J. Lucier, M. Kallergi, W. Qian, R. A. DeVore, R. A. Clark, E. B. Saff, L.P. Clarke, "Wavelet compression and segmentation of digital mammograms," *J. Digit Imaging Feb*; 7(1):27:38 (1994).
18. A. Maeder, M. Deriche, "Establishing perceptual limits for medical image compression," *Image Perception and Performance, Proc. of SPIE, Vol. 4324*, 204-210 (2001).
19. H. E. Johns, J. R. Cunningham, *The Physics of Radiology*, 4th. ed. (Thomas, Springfield, IL, 1983).
20. R. K. Swank, "Absorption and noise in x-ray phosphors," *J. Appl. Phys.* 44, 4199-4203 (1973).
21. H. Fujita, D. Y. Tsai, T. Itoh, K. Doi, J. Morishita, K. Ueda, and A. Ohtsuka, "A simple method for determining the modulation transfer function in digital radiography," *IEEE Tran. Med. Imaging* 11, 34-39 (1992).
22. R. Aufrichtig, "Comparison of low contrast detectability between a digital amorphous silicon and a screen-film based imaging system for thoracic radiography," *Med. Phys.* 26(7), 1349-1358 (1999).

23. M. Ishida, K. Doi, L. Loo, C. E. Metz, J. L. Lehr, "Digital image processing: Effect on detectability of simulated low-contrast radiographic patterns," *Radiology* 150, 569-575 (1984).
24. R. F. Wagner, D. G. Brown, and M. Pastel, "Application of information theory to the assessment of computed tomography," *Med. Phys.* 6, 83-94 (1979).
25. A. E. Burgess, F. L. Jacobson, P. F. Judy, "Human observer detection experiments with mammograms and power-law noise," *Med. Phys.* 28(4), 419-436 (2001).
26. Stephen Welstead, *Fractal and Wavelet Image Compression Techniques*, SPIE-The International Society of Optical Engineering, (1999).
27. J. E. Tkaczyk, J. LeBlanc, R. Nevin, G. Kautz, D. Albagli, J. Sandrik, and P. R. Granfors, "Modeling the x-ray energy characteristics of DQE for full-field digital mammography," *Proc. SPIE* 4320, 570-581 (2001).
28. D. P. Chakraborty, G. T. Barnes, "Signal-to-Noise ratio considerations in Radiographic Imaging", *Med. Phys.* 1983 Jul-Aug,10(4):467-469.
29. J. T. Dobbins, D. L. Ergun, L. Rutz, D. A. Hinshaw, H. Blume, and D. C. Clark, "DQE(f) of four generations of computed radiography acquisition devices," *Med. Phys.* 22, 1581-1593 (1995).
30. W. Hillen, W. Eckenbach, P. Quadflieg, and P. Zaengel, "Signal-to-noise performance in cesium iodide x-ray fluorescent screens," *Proc. SPIE* 1443, 120-131 (1991).

31. K. Cranley, B. J. Gilmore, G. W. A. Fogarty, and L. Desponds, *Catalogue of diagnostic x-ray spectra and other data*, Report No. 78, Institute of Physics and Engineering in Medicine.
32. R. Birch, and M. Marshall, "Computation of Bremsstrahlung x-ray spectra and comparison with spectra measured with a Ge(Li) detector," *Phys. Med. Biol.* 24, 505-517 (1979).
33. A. E. Burgess, "Comparison of receiver operating characteristic and forced choice observer performance measurement methods," *Med. Phy.* 22(5), 643-655 (1995).
34. K. Ohara, K. Doi, C. E. Metz, M. L. Giger, "Investigation of basic imaging properties in digital radiography. 13. Effect of simple structured noise on the detectability of simulated stenotic lesions," *Med. Phy.* 16(1), 14-21 (1989).
35. E. Cendre, P. Duvauchelle, G. Peix, J. Y. Buffiere, and D. Babot, "Conception of a high resolution x-ray computed tomography device; Application to damage initiation imaging inside materials," 1st World Congress on Industrial Process Tomography, Buxton, Greater Manchester, April 14-17 (1999).
36. <http://www.carroll-ramsey.com/scintillatorapps.htm>
37. C. Herrmann, E. Buhr, D. Hoeschen, S. Y. Fan, "Comparison of ROC and AFC methods in a visual detection task," *Med. Phy.* 22, 643-655 (1993).
38. P.C. Bunch, "The effects of reduced film granularity on mammographic image quality," *Proc. SPIE* 3032, 302-317 (1997).
39. P. C. Bunch, "Advances in high-speed mammographic image quality," *Proc. SPIE* 3659, 120-130 (1999).